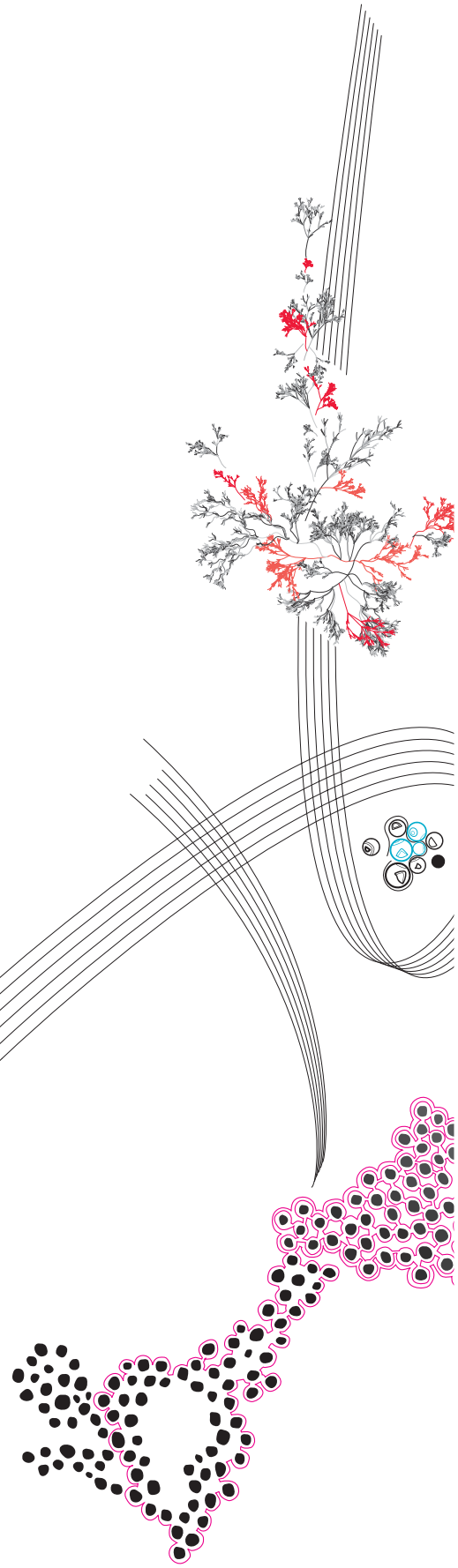

MSc Mechanical Engineering
Master's Assignment

On the Relation Between Microstructure and Transverse Electrical Resistivity of Unidirectional Composites

An Evaluation Statistical Spatial Descriptors and a Quasi-3D Resistor Network Model

Hafidz El Amien Noor Pamungkas
s2842351

Exam Committee:
Chair: prof.dr.ir. R. Akkerman
Internal Supervisor: dr.ir. W.J.B. Grouve
Internal member: dr. M.I. Abdul Rasheed
Internal member: ir. W. J. Schuttert

October 2024

Department of Production Technology
Faculty of Engineering Technology
University of Twente

UNIVERSITY OF TWENTE.

Abstract

Over the past century, advancements in material science and technology have led to the development of materials with improved performance and reduced costs. Composite materials have shown promising performance in the aerospace industry application due to their high strength-to-weight ratio and excellent fatigue resistance. Thermoplastic composites are gaining more interest over their thermoset counterparts due to their melt processability, which offers advantages in manufacturing and assembling large parts through cost-effective fusion bonding processes. Induction welding is an attractive assembly technology that uses the melt processability of the thermoplastic matrix to bond multiple parts. This technology uses an induction coil to generate heat in a workpiece by means of eddy currents, which rely on the conductive network of fibres within the composite material.

Simulating the heating mechanism during the induction welding would provide significant value in process window development and optimisation of the process. One of the input parameters in the simulation is the anisotropic conductivity of the composite material. While the conductivity in the fibre direction can be estimated using the rule of mixture, the in-plane transverse and through-thickness conductivity needs to be characterised experimentally. It has been observed that in these particular directions, the morphology of the material, which includes the fibre volume fraction and the quality of the fibre-to-fibre contact, plays an essential role in the low conductivity value obtained from the measurement.

This study focuses on the correlation between the fibre distribution in a 2D cross-sectional micrograph and the electrical conductivity of a unidirectional composite in the transverse direction. Several statistical descriptors were used to quantify the fibre distributions as obtained from microscopy. In addition, a quasi-3D resistor network was created based on the micrographs. The findings from this study suggest that 2D statistical spatial analysis is inadequate for assessing the correlation between the morphology and the measured electrical conductivity since it is limited to local fibre arrangements and short to medium-range distribution. Furthermore, the quasi-3D microstructure-based resistor network model seems to show a good preliminary approach to estimate the equivalent resistance value by considering threshold parameters based on inter-fibre distance and local fibre volume fraction within the microstructure. Further improvements to the model are necessary to build a more reliable model and ensure that the estimated resistance values are accurate.

Contents

Chapter 1

Introduction

1.1 Background

Over the past century, significant advancements have been made in the field of material science and technology. Many efforts have been spent on developing materials with improved performance and reduced costs. Due to their high strength-to-weight ratio and excellent fatigue resistance, carbon fibre-reinforced polymers (CFRP) are being increasingly used as a structural material in many applications.

Traditionally, thermoset composites (TSCs) have predominantly been found in applications within the modern aerospace sector for manufacturing aircraft parts, such as aircraft skin and structural components. Recently, however, the industry has shown a great interest in incorporating thermoplastic composites (TPCs) [1] as the material to manufacture both skin and stiffener using unidirectional (UD) TPCs tapes, mainly due to the possibility of automating the manufacturing and the assembly process. Opting for TPCs over the TSCs counterparts has numerous advantages, including high impact resistance, improved toughness, and infinite shelf life [3]. Additionally, a key benefit of TPCs material, in contrast to their TSCs counterparts, is the possibility of material assembly through fusion bonding, eliminating the necessity to use adhesives or mechanical fasteners.

In principle, fusion bonding, also known as welding, involves local heat generation at the contact interface, followed by cooling or consolidating under pressure. Currently, the most developed welding technologies for joining the TPCs part are ultrasonic welding, resistance welding, and induction welding. Out of these technologies, induction welding (IW) is considered an attractive option as no susceptor material is required at the weld interface. Moreover, the process is suitable for high-rate manufacturing and is highly automatable.

Figure 1.1a schematically illustrates the induction welding process. A coil is brought in close proximity to the assembly and then used to generate an alternating magnetic field. Consequently, the magnetic field generates an eddy current in the electrically conductive network of carbon. The inherent resistance of the fibre causes the energy to be lost in the form of heat, allowing the material to melt and be further processed. In order to generate the heat in the composite part, the eddy currents are form in a closed-loop circuit at a ply level, as schematically shown in Figure 1.1b. In the case of UD TPCs, multiple plies are needed to form the closed-loop circuit.

During induction welding, three heating mechanisms are identified, namely Joule loss (or fibre heating), junction heating (or dielectric hysteresis), and contact heating [1]. Fibre heating is due

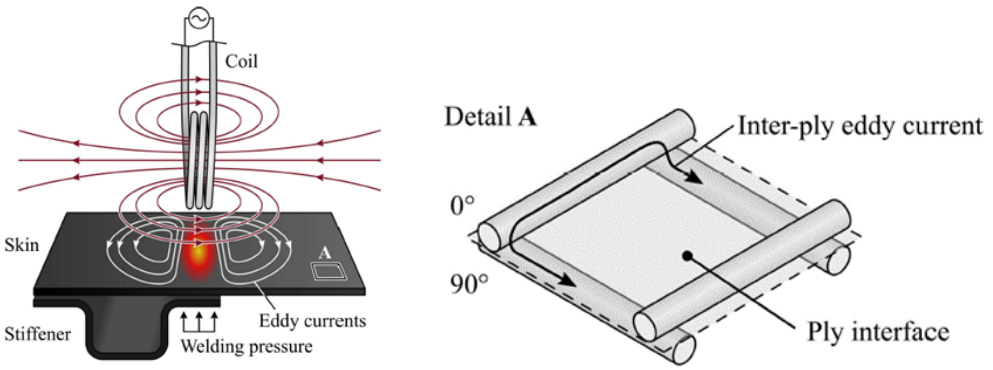

(a) Induction heating of CFRP laminate (b) Interply eddy current on a closed loop conductive fibre path

Figure 1.1. Schematic of induction welding of CFRP laminate [2]

to the inherent resistance of the fibre itself, which depends highly on its geometrical and electrical properties, including length, resistivity, and cross-sectional area. Dielectric hysteresis occurs due to a potential difference between fibre separated by a thin layer of matrix material, generating a capacitor effect. Lastly, contact resistance takes place when there is a high level of contact between fibres. In the case of Figure 1.2, the eddy current flows through the conductive path along the fibre and the fibre contact.

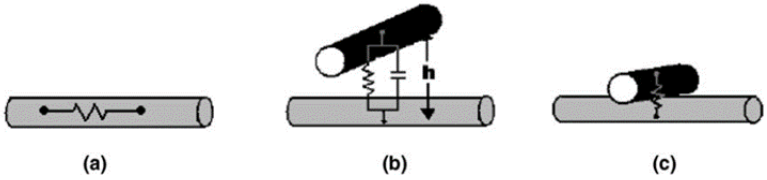

Figure 1.2. Heating mechanism during induction heating of CFRP laminate [3]

As can be seen from Figure 1.1b, the eddy current will be generated relatively easily in a cross-ply or woven laminate due to the incidence of fibre-fibre contact, which consequently provides electrically conductive loops. However, this would not be the case for UD composites. Generating eddy currents, thus, the internal heat, is notably more challenging in UD composites because all fibres are oriented in the same direction. As such, the eddy currents have to travel perpendicular to the fibre direction, which is difficult as it depends on fibre-fibre contacts.

In the transverse and through-thickness directions, the flow of current is influenced by the occurrence of fibre-to-fibre contacts caused by morphological occurrences, such as fibre clustering and fibre waviness. The mechanism of current flow due to fibre-to-fibre contact is schematically shown in Figure 1.3. Fibre-fibre contacts in the microstructure create a conductive pathway for the current to flow. Therefore, a limited number of contact incidences in both directions results in low conductivity, hindering the formation of the conductive pathways for the current to flow. These limitations resulted in four to five-order lower conductivity in both directions compared to the conductivity in the longitudinal direction. Thus, the electrical conductivity of TPCs is highly anisotropic [3]–[6].

Furthermore, the electrical conductivity is partly governed by the fibre volume fractions (FVFs) within the microstructure. In the context of the electrical conductivity of UD CFRP, a higher FVFs value might be related to higher transverse conductivity since it affects the probability of

fibre contact incidence. This is because the conductive pathways provided by the incidence of fibre contact become more prevalent as their FVFs increase [7].

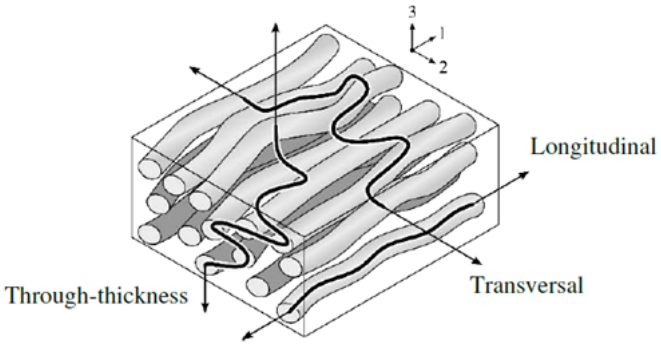

Figure 1.3. Schematic of longitudinal, transverse and through-thickness current flow in a UD composite [5]

1.2 Problem Statement

A numerical model capable of simulating the heating mechanism during the IW process of TPCs material would provide a significant value in process window development and optimisation of IW. As mentioned in Section 1.1, the heating mechanism is contributed by the formation of the eddy current within the part of the joining interface when subjected to an alternating magnetic field. The formation of eddy current in UD composite, particularly in transverse and through-thickness directions, is influenced by the occurrence of fibre-to-contact, which results in highly anisotropic electrical conductivity. Hence, the anisotropic electrical conductivity of the composite material is an essential input to the simulation of heat generation during the IW process.

While the electrical conductivity in the fibre direction can be well estimated using the rule of mixtures approach, the same cannot be said for the transverse conductivity. As a consequence, the in-plane and through-thickness conductivity are characterised experimentally. Buser et al. [5] conducted a measurement of electrical conductivity for Solvay C-PEKK and Toray C-PEKK materials. The measurement result from both materials showed that the transverse conductivity of specimens taken from the same laminate varies considerably. In contrast, the conductivity of specimens in the fibre direction is relatively consistent. The variations observed in the measurement are due to the stochastic nature of the fibre-to-fibre contacts.

The morphology of the materials, including fibre clustering and, consequently, the FVFs, play an essential role in the electrical conductivity in transverse and through-thickness directions, as these parameters affect the amount of fibre incidence in both directions. This research will focus on the fibre distribution and morphology in the microstructure of the UD TPCs in relation to the value of electrical conductivity in transverse and through-thickness directions.

1.3 Research Objective and Approach

The primary objective of this research is to evaluate the correlation between the morphology of a 2D cross-sectional micrograph and the electrical conductivity of UD TPCs in transverse and through-thickness directions. The traditional method relying on 2D micrographs provides limited insight into the complex microstructure features that influence conductivity as they do not capture the fully

three-dimensional stochastic nature of the fibres. To address this limitation, the second objective is to develop a microstructure-based quasi-3D resistor network that can estimate the electrical resistance of the material. This approach aims to bridge the gap between 2D morphological analysis and a more comprehensive understanding of electrical properties, thereby improving the estimation of resistance in anisotropic materials.

This research will consider two analyses: 2D statistical spatial characterisation and quasi-3D resistor network. Firstly, this research will be carried out by reviewing the literature regarding the commonly used method to quantitatively analyse the morphology of a 2D cross-section micrograph of UD TPCs, followed by reviewing the currently developed resistor network model in the UD TPCs. Image processing techniques will be used to analyse the fibre distribution and to evaluate the statistical spatial characterisation. The microstructure feature will then be used as an input to generate the quasi-3D resistor network and solve for the equivalent resistance.

The results obtained through the micrograph analysis and modelled resistor network can provide a better understanding of the relation between the morphology of the fibre and the measured electrical conductivity. The analysis would also help to determine whether the estimated value of the resistance of UD TPCs is comparable with the experimental result. The method presented in this work can be used as a toolbox to analyse the fibre distribution in the cross-section and estimate material resistance in relation to conductivity in transverse and through-thickness directions for UD TPCs materials.

Chapter 2

Theory and Literature

This chapter provides background information and theoretical knowledge on topics that are relevant to this research. Section 2.1 describes the anisotropic properties of UD TPCs in regard to the electrical conductivity in the principle direction of the material. Section 2.2 explained the statistical descriptor to evaluate the spatial characterisation of a 2D cross-sectional micrograph. Subsequently, the principle of generating a general network is described in Section 2.3, followed by the description of the method to solve a node-voltage analysis in a resistor network in Section 2.4. This chapter ends with Section 2.5, which provides a brief explanation to characterise the electrical conductivity in transverse and through-thickness directions utilizing a six-probe method.

2.1 Anisotropic Resistivity and Conductivity

Electrical resistivity, denoted as ρ, is an intrinsic property of a material that represents the ability of a material to resist a current flow. A material with lower resistivity allows more current to flow within the material. The resistivity of the material can be calculated with the following equation:

$$\rho = R\frac{A}{L}, \tag{2.1}$$

where ρ [Ωm] is the electrical resistivity, R [Ω] is the electrical resistance of a specimen with cross-section A [m^2] and length L [m]. Figure 2.1 shows a volume of a material relating the material characteristic to the calculation of resistivity. The resistance, R, of a material is dependent on the geometry of the material dimension, meaning that if the length of the material increases, the resistance will increase proportionally. Hence, the resistivity, ρ, is independent of the length or the form of the material.

The electrical conductivity of a material, represented by σ, refers to the ease of current flow through a material, and it is defined as the inverse of the resistivity. This simply means that a high resistivity is the same as a low conductivity, and a low resistivity is the same as a high conductivity. The relation between resistivity and conductivity can be written as:

$$\sigma = \frac{1}{\rho}. \tag{2.2}$$

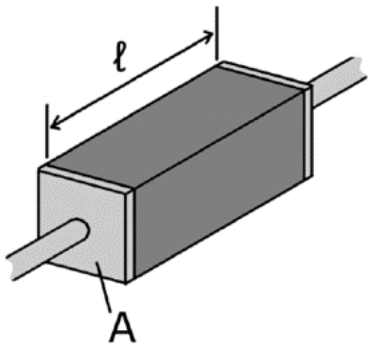

Figure 2.1. Schematic of volume of a material [3]

The conductivity of a composite is a directional property and highly anisotropic. This means that the conductivity of a composite can be written in tensor form (see Equation 2.3). In its basic form, the off-diagonal terms are non-zero. The subscripts 1, 2, and 3 represent the conductivity in three principal material directions: the longitudinal conductivity in the fibre, the transverse conductivity in-plane transverse to the fibre, and the through-thickness conductivity in out-of-plane directions, respectively. In the case of anisotropic material, the relation between the resistivity and conductivity can be written in general terms as $\bar{\sigma}=\bar{\rho}^{-1}$ and the properties aligned with the material principal direction still holds, e.g. $\sigma_1=1/\rho_1$.

$$\bar{\sigma} = \begin{bmatrix} \sigma_1 & 0 & 0 \\ 0 & \sigma_2 & 0 \\ 0 & 0 & \sigma_3 \end{bmatrix}. \tag{2.3}$$

It has been stated the electrical conductivity of UD CFRP is governed by the morphology of the material, which includes, for example, the fibre volume fraction, fibre orientation, and the number and quality of the contacts between the fibres. This is especially true when considering the conductivity of transverse (σ_2) and through-thickness (σ_3). As visualised in Figure 2.2, the fibres inside the material are not perfectly straight and parallel to each other. Fibre waviness can create a conductive pathway between neighbouring fibres for current to flow in transverse and through-thickness directions. The limited number of contact points in the transverse and through-thickness direction makes the conductive path length for the current to traverse longer, reducing the effective area for the current flow. Furthermore, the electrical resistance caused by the fibre-to-fibre contacts is higher than the inherent resistance of the fibre. Therefore, the sum of resistance at these junctions, coupled with the extended lengths of these pathways, results in an approximate difference of four orders of magnitude between the longitudinal direction and both the in-plane and through-thickness transverse directions [4]–[6].

Previous work [4]–[6] proved that the longitudinal conductivity (σ_1) can be predicted using the Rule of Mixture (RoM):

$$\sigma_1 = f\sigma_f + (1-f)\sigma_m \approx f\sigma_f, \tag{2.4}$$

where σ_1 [S/m] refers to the longitudinal conductivity, f refers to the fibre volume fraction, and the subscripts f and m represent the fibre and matrix, respectively. This equation could provide

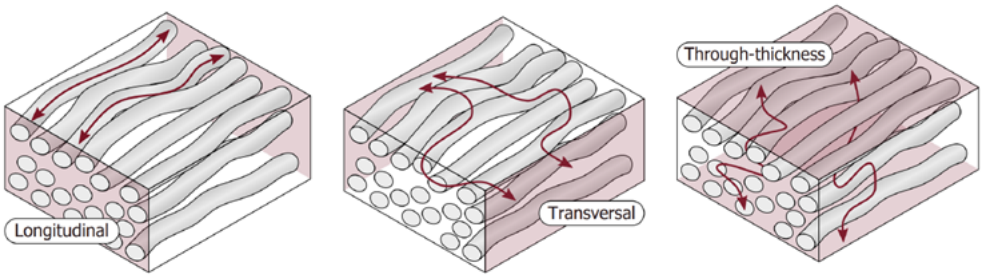

Figure 2.2. Conductivity in three principle directions of a UD composite [3]

a relatively fast and accurate estimation of the properties, with a simplification where the matrix materials are considered as an insulator (i.e. σ_m=0). However, this expression does not give an accurate estimation of the conductivity in the transverse and through-thickness directions. To the author's knowledge, the relation for predicting those conductivity does not yet exist.

2.2 Statistical Spatial Characterization

Microscopic characteristics play a crucial role in understanding and modelling the performance of UD composite. Factors such as size and shape variations, as weel as the spatial arrangement of individual fibres at a local level can indeed influence the estimation of the effective properties of the materials [8]. In recent years, the characterisation of microstructures of fibre-reinforced composites has been performed using various image-analysis techniques of a cross-sectional micrograph obtained from optical microscopy or scanning electron microscopy [7], [9], [10]. In this research, image analysis techniques are employed to quantitatively analyse the statistical fibre distribution of a 2D cross-section micrograph of a UD composite. and subsequently analyse the statistical data to study the correlation with the conductivity obtained using experimental measurement.

This work employs four statistical descriptors to quantify the short and long-range interaction of fibres, namely the nearest neighbour distance, nearest neighbour orientation, Ripley's K Function, and pair distribution function [7], [11], [12]. These statistical descriptors will be elaborated further in the following sections.

2.2.1 Nearest Neighbour Distance (NND)

The nearest neighbour distance (NND) is defined as the shortest distance between a reference fibre and its closest neighbouring fibres [13]. In general, the distribution of the nearest neighbour distances is analyzed using a probability density function (PDF) which describes the frequency of a particular distance within the observed area. The PDF of the nearest neighbour distance provided information on the inter-fibre distance and is used to explain the feature of fibre arrangement and the possibility of contact between each fibre. The distribution can provide information regarding the degree of clustering of the fibre distribution within a given space, which is typically shown as a sharp peak in the PDF plot at a specific distance value.

The shortest distance between the reference and its neighbouring fibre can be computed using the nearest neighbour algorithm (NNA) provided by Scipy module with cKDTree function in Python [14].

2.2.2 Nearest Neighbour Orientation (NNO)

The nearest neighbour orientation (NNO) is defined as the distribution of the orientation of the shortest line which connects the centres of the reference fibre with its nearest neighbour. In general, NNO is described using cumulative distribution function (CDF) and accounts for all fibres inside the boundary area. The CDF represents the total number of fibres which have the nearest neighbour oriented along a particular direction [15]. As presented in Figure 2.3, NNO is determined by calculating the rotation angle counterclockwise to the line from the reference fibre to its nearest fibre with respect to the x-axis. The orientation angle between the reference and its neighbouring fibre can be computed simply using the inverse tangent function provided by Numpy in Python [16]. For the distribution of a completely spatial random (CSR) pattern, the plot of the CDF is a straight diagonal line, suggesting that there is an equal probability of occurrence for any orientation. In the case of a periodic pattern where the distribution of the orientation is concentrated at a certain angle, the CDF plot will be a stair-shape, giving a deviation from the diagonal line.

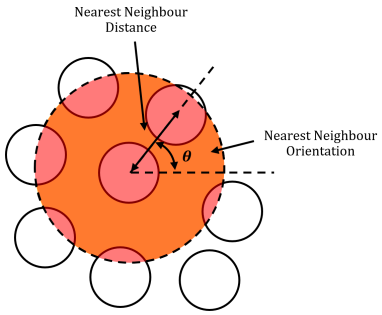

Figure 2.3. Schematic diagram of the nearest neighbour analysis

2.2.3 Ripley's K Function

The Ripley's K Function, also known as the second-order intensity function, measures the spatial dependence of points within a certain radius [13]. The function quantifies the ratio of the number of fibres within a radius distance, r, for an arbitrary fibre against the number of fibres that lie in a unit area, as illustrated in Figure 2.4. It helps to determine whether the point pattern is clustered, randomly distributed, or uniformly spaced at a particular distance. The formula to estimate Ripley's K Function is the following:

$$K(r) = \frac{A}{N^2} \sum_i \sum_{j \neq i} \frac{I(d_{ij} \leq r)}{w(i,j)}, \tag{2.5}$$

where A represents the area of the RVE, N is the total number of fibre in the RVE, I is an indicator function that equals 1 if the distance between the reference fibre (i) and observed fibre (j), d_{ij}, is less than or equal to the radius distance, r, and 0 otherwise. The weight function $w(i,j)$ takes the value of 1 if the circle centred on i and passing through fibre j is completely inside the window. Otherwise, $w(i,j)$ is the ratio of the circumference contained within the RVE to the whole circumference of the circle. The spatial pattern or distribution of the fibre is typically compared with the CSR pattern. For a CSR pattern, which is also called Poisson distribution, the Equation 2.5 can be simplified as

$$K_{CSR}(r) = \frac{\pi h^2 N/A}{N/A} = \pi h^2. \tag{2.6}$$

Comparing the $K(r)$ and K_{CSR} curves can give a better understanding of the fibre distribution behaviour. According to Yang et al. [17] and Melro et al. [18], the comparison between these two curves indicates a degree of randomness between the observed fibre distribution and a random (Poisson) distribution. If the $K(r)$ curve lies below the K_{CSR} curve, it shows that the fibre is more regularly distributed than random. On the other hand, fibre clustering appears when the curve of $K(r)$ lies above the K_{CSR} curve. When the fibre has a periodical distribution (square of hexagonal distribution), the $K(r)$ curve will have a stair-shaped curve, similar to the CDF.

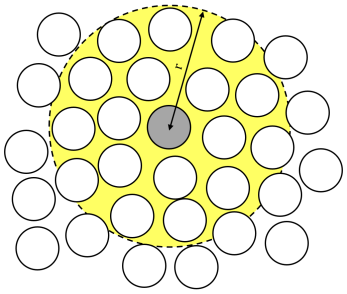

Figure 2.4. Schematic diagram of Ripley's K function analysis

2.2.4 Pair Distribution Function

The pair distribution function, $g(r)$, also known as the radial distribution function, quantifies the probability of finding a number of fibres lying within an annular region of inner radius, r, and outer radius, $r + dr$, over the average number of fibres within a unit area. This analysis is schematically shown in Figure 2.5. The function can be expressed as the following

$$g(r) = \frac{1}{2\pi N_a \mathrm{d}r} \cdot \frac{1}{N} \sum_{i=1}^{N} n_i(r) = \frac{1}{2\pi r} \frac{\mathrm{d}K(r)}{\mathrm{d}r}, \tag{2.7}$$

where $\mathrm{d}K(r)$ and $n_i(r)$ are defined as the average number and the total number of fibres lying within an annulus of inner radius, r, and outer radius, $r + dr$, respectively, N_a is the number of fibres per unit area [13].

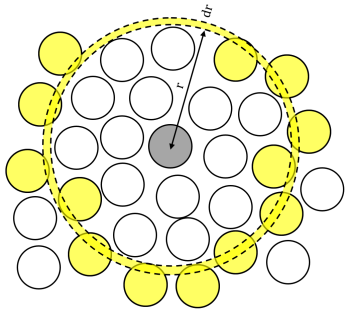

Figure 2.5. Schematic diagram of pair distribution function analysis

The distribution function, $g(r)$, presents the same statistical information as the $K(r)$ but in a way that is easier to understand. It can be seen that by substituting Equation 2.5 to Equation 2.7, the Poisson point distribution will make $g(r) = 1$ for every distance measured, which indicates that the

fibre distribution is completely random. The curve of $g(r)$ that is larger than 1 indicates that there is fibre clustering at distance r, meaning that there are more points at this distance than expected under randomness. On the other hand, the degree of regularity presents when the curve of $g(r)$ is below 1. Therefore, $g(r)$ must have a value close to 1 as distance r increases for a fibre distribution to be considered statistically valid and random.

2.3 Graph Theory

Graph theory is one of the most important fields in mathematics and computer science that focuses on the study of graphs, a structure that models the interactions between pairs of objects [19]. Graph theory is often used as a way to represent the structural information of topological networks. In the context of this work, it is used to represent the connectivity or interaction of fibre networks within a given space. As illustrated in Figure 2.6, a graph consists of a collection of vertices, also called nodes, with corresponding sets of edges. Formally, a graph can be written as $G = (V, E)$ where V is a set of nodes and E is the corresponding set of edges.

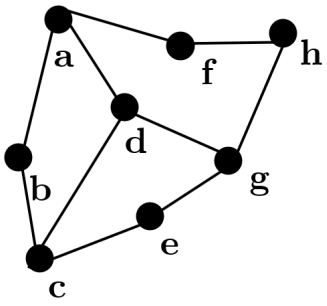

Figure 2.6. Schematic diagram of graph

There are two main types of graphs, namely undirected and directed graphs. The edges of a directed graph have a constraint in one direction, pointing from the start node u, to the target node v. On the other hand, the edges of an undirected graph are considered the same when it points from node u to node v, and vice versa, such that $(u, v) \in E \Leftrightarrow (v, u) \in E$. Additionally, the edges of the graph can be assigned with a particular value that represents the costs of interaction between the start and target nodes.

According to several authors [20], [21], a polymer composite can be modelled as a resistor network for simulation. By utilising the characteristic of a graph, the fibre interaction in the microstructure is modelled as an equivalent electrical network to solve the equivalent resistance within a given window using a node-voltage analysis. In the case of the work presented here, the fibre centres are represented by nodes, and edges represent the contact between adjacent fibre. The derivation of node-voltage analysis is explained in Section 2.4, and the implementation of the graph theory into the model is elaborated further in Chapter 4. The graph network can be implemented using a function provided by the NetworkX library in Python [22].

2.4 Node-Voltage Analysis

In node-voltage analysis, Kirchoff's current law (KCL) is applied to derive the equation for each node in the circuit. The principle of the analysis is to determine the voltage at every node. In this

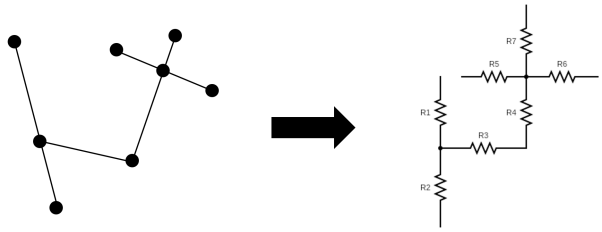

Figure 2.7. Transforming a graph network into electrical circuit

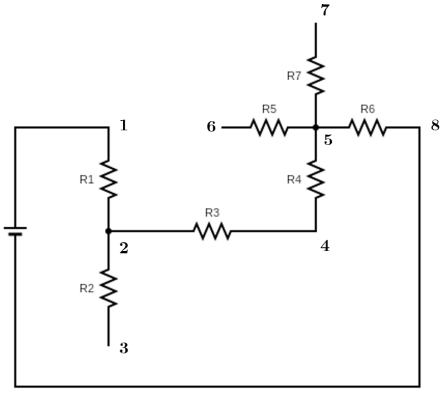

Figure 2.8. Example of a resistor network

methodology, each edge from the graphs is treated as a resistor, the reference and target nodes are applied with a particular current value, and then the voltage of these two nodes is solved to obtain the resistor network's equivalent resistance.

The process of transforming a graph into a resistor network is schematically shown in Figure 2.7. Note that the edges in the graph have been assigned to a value that corresponds to the resistance in value in the network. Subsequently, the following matrix equation can be formed:

$$[G_N][\bar{V}_N] = [\bar{I}_N], \tag{2.8}$$

where $[G_N]$ is the conductance (inverse of resistance) matrix, $[\bar{V}_N]$ is a column vector that contains the nodal voltages, and $[\bar{I}_N]$ is a column vector of all nodal currents. In the case of an electrical circuit with only a source and resistor, the conductance matrix is symmetric. In order to illustrate the process of derivating the set of equations, the resistor network from Figure 2.8 will be analysed. In the example below, the boundary condition of the circuit would be node 1, which is connected to the current source and node 8, which is connected to the ground (voltage equal to zero).

The current vector, $[\bar{I}_N]$, is formed by the algebraic sum of the currents flowing in and out of a node, and according to KCL, the total current flowing in a node is equal to the current flowing out. Hence, the total algebraic sum of the current in all nodes would be 0, except for the source node. The numbering of the nodal is used to arrange the vector in the correct order. Furthermore, the elements of the conductance matrix can be filled by considering the principle of nodal analysis. According to the nodal analysis, the diagonal terms of $[G_N]$ are filled by adding all of the conductance of the resistors connected to each node, which is defined as the inverse of the resistance value.

As shown in Equation 2.9, for instance, the first row of $[G_N]$ shows a relation between the conductance, nodal voltage, and nodal current for node 2. Since node 2 is connected to node 1, 2, and 4, which correspond to the conductance values of $1/R_1$, $1/R_2$, and $1/R_3$, respectively, then by summing all conductance values, can we obtain the first diagonal element of $[G_N]$. The non-diagonal elements of the i-th row of $[G_N]$ are 0, except for the columns corresponding directly to a node connected to node i via a resistor. The value for this element would be the negative of

the conductance of the connected resistor. Note that this is the case for source and resistor-only circuits, and the conductance matrix is symmetric about the diagonal. Once the conductance matrix $[G_N]$ has been filled, the system of equations can be solved for the nodal voltages by multiplying the inverse of the conductance matrix, $[G_N]$, and the current vector $[\bar{I}_N]$, according to Equation 2.9. The potential difference between the source node and the ground can be utilised to calculate the value of the equivalent resistance within the network.

$$\begin{bmatrix} \frac{1}{R_1}+\frac{1}{R_2}+\frac{1}{R_3} & -\frac{1}{R_2} & -\frac{1}{R_3} & 0 & 0 & 0 \\ -\frac{1}{R_2} & \frac{1}{R_2} & 0 & 0 & 0 & 0 \\ -\frac{1}{R_3} & 0 & \frac{1}{R_3}+\frac{1}{R_4} & -\frac{1}{R_4} & 0 & 0 \\ 0 & 0 & -\frac{1}{R_4} & \frac{1}{R_4}+\frac{1}{R_5}+\frac{1}{R_6}+\frac{1}{R_7} & -\frac{1}{R_6} & -\frac{1}{R_5} \\ 0 & 0 & 0 & -\frac{1}{R_6} & \frac{1}{R_6} & 0 \\ 0 & 0 & 0 & -\frac{1}{R_5} & 0 & \frac{1}{R_5} \end{bmatrix} \begin{bmatrix} V_2 \\ V_3 \\ V_4 \\ V_5 \\ V_6 \\ V_7 \end{bmatrix} = \begin{bmatrix} I_s \\ 0 \\ 0 \\ 0 \\ 0 \\ 0 \end{bmatrix} \tag{2.9}$$

2.5 Electrical Conductivity Characterisation

This work will employ the six-probe method as the basis for characterising the electrical conductivity along two principle directions of the fibre composite specimen. As schematically presented in Figure 2.9, the direct current (DC) is applied over the width of the specimen at Probe A and expelled at Probe B. This will yield a uniform current flow across the width but might be non-uniform across the thickness, t. Subsequently, the four probes that are on top and bottom of the specimen are used to sample the voltage response or the distribution of the non-uniformity of the current on the top and bottom side of the specimen, V_t and V_b, respectively. The difference measured betweenV_t and V_b allows the determination of the in-plane conductivity σ_x and through-thickness conductivity, σ_z. The data reduction of the probe method will be elaborated further in Chapter 3.

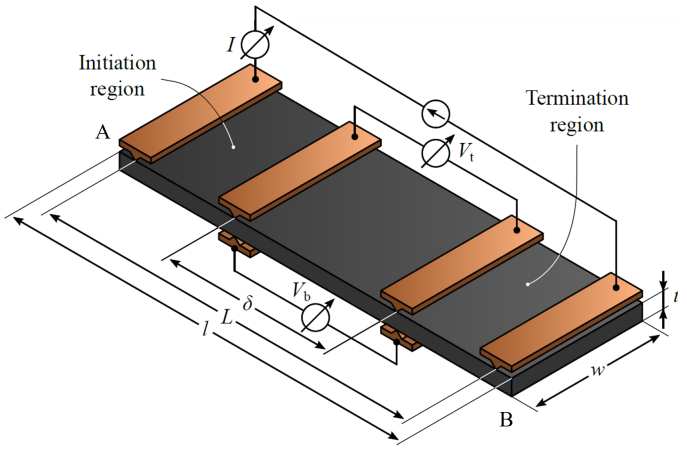

Figure 2.9. Schematic of the six-probe method [2]

Chapter 3

Experimental Work

This chapter describes the methodology to analyse the microstructure and the electrical conductivity of specimens in transverse and through-thickness directions. Section 3.1 describes the material investigated in this study and the manufacturing process of the UD laminate. Section 3.2 elaborates on the characterisation process performed using the six-probe method with the transverse sample, followed by the description of the COMSOL model used for simulation to obtain the conductivity value. This chapter ends with Section 3.3 that elaborates the process of analysing the microstructure, including how the micrographs are examined, and image analysis techniques, consisting of fibre centre extraction, fibre radii calculation, and Voronoi tessellation analysis steps.

3.1 Material and Specimen Manufacturing

This work investigates two pre-impregnated composite materials from two material suppliers: Toray TC1200 and Solvay APC. The Toray material samples consist of AS4 unidirectional carbon fibre as reinforcement with PEEK matrix material. Meanwhile, the Solvay material samples are made from AS4D carbon fibre using PEKK matrix material. Both materials samples have 59% fibre volume fraction with a fibre areal weight of 145 g/m^2 and a fibre conductivity of 59 kS/m [5].

The unidirectional laminate has been manufactured using a hot consolidation press present at the TPRC. For each laminate, the plies have been cut to the 12 x 12 in^2 size with $[0]_{16s}$ fully UD layup and subsequently pressed using a picture frame mould. The plies are stacked on top of each other and flipped and rotated by 180° after half of the thickness of the laminate to create symmetry. This means that half of the total plies are aligned in the same direction with their ends are reversed.

During the manufacturing process, minor variations in fibre placement or resin distribution can occur along the tape. The choice of stacking is to account for any potential inconsistencies in fibre or resin density along the length of the tape. Rotating the ples can ensure that any variations in the fibre or resin distribution across the length of the laminate are averaged out, which improves the overall uniformity and consistency of distribution across the laminate. The plies are then consolidated according to the parameters provided in Table 3.1.

From each laminate, a total of 20 specimens were precision milled for electrical conductivity measurement. After milling, the specimens were cleaned thoroughly from the carbon dust and cut residue at the corners. The dimensions of the specimens were 55 mm in length and 15 mm in width. The fibres were oriented in the width direction of the specimen. Ten specimens were obtained from the starting end (left side) of the laminate, and the rest were taken from the other

Material	Consolidation cycle			
	Temperature	Pressure	Dwell	Cooling rate
Toray C/PEKK	385°C	20 bar	20 min	5°C/min
Solvay C/PEKK	380°C	20 bar	30 min	5°C/min

Table 3.1. Consolidation parameter of 32-ply laminates

finished end (right side), as referred in Figure 3.1. The choice of this location was to observe how the variation of fibre distribution at the edge region of the laminate might influence the measured electrical conductivity of the specimen, by analysing the micrograph of every specimens. Due to time limitations, however, only one micrograph was analyzed from a single specimen. As a result, a comprehensive analysis of the fiber distribution across all specimens could not be performed. The thickness of each specimen was measured with a micrometre in a 2-point grid.

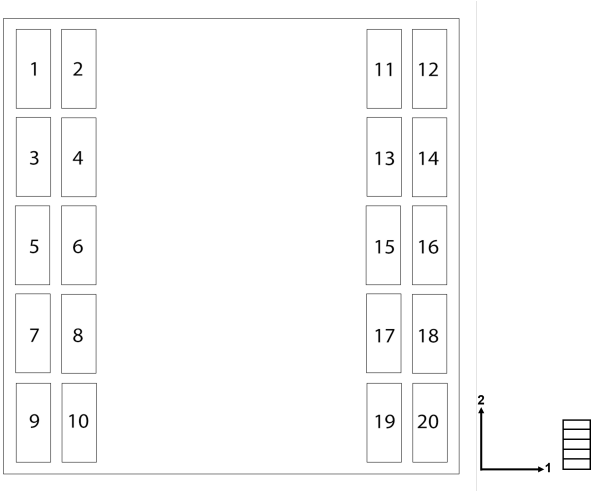

Figure 3.1. Sketch of laminate for cutting the specimen with specified number and location

3.2 Six Probe Characterization

The six-probe method is used to characterise the transverse conductivity of the specimen. The six-probe characterisation has been briefly described in Section 2.5. This method will be implemented using the transverse six-probe specimens, where the fibres are oriented along the width of the specimen. With these specimens, the transverse and through-thickness conductivities can be characterised. The six-probe setup and the data reduction using COMSOL model will be elaborated in the following subsections.

3.2.1 Six Probe Setup

The conductivity characterisation of the transverse specimens was performed by implementing the six-probe method fixture that was developed and manufactured by previous researchers at the TPRC [3], [6], The six-probe setup for the specimens is depicted in Figure 3.2. The setup consists of three parts: a top electrode assembly, a bottom electrode assembly, and two toggle clamps.

For all measurements, the spacing of inner electrodes, δ, and outer electrodes, L, were set to 20 mm and 50 mm, respectively. To ensure that the specimen was fixed at the centre of the probes,

an electrically insulating alignment bracket was 3D-printed from polylactic acid (PLA). The toggle clamps were installed to establish the contact pressure between the specimens and the probes.

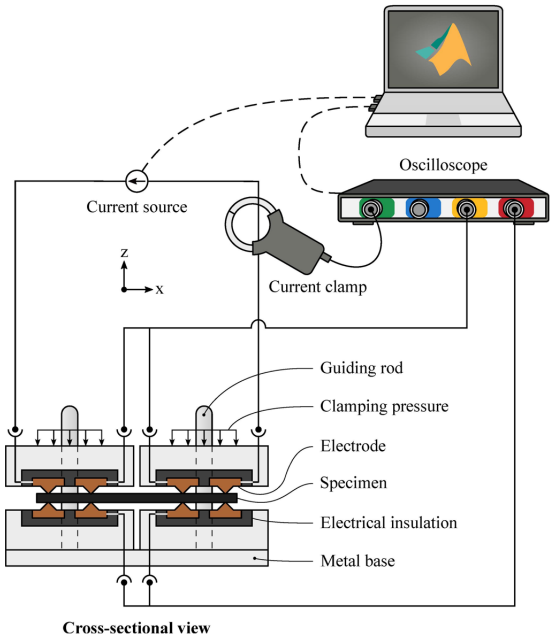

Figure 3.2. Six probe setup. Used with permission

A Tenma 72-13360 DC power supply was programmed to perform a voltage sweep from 5V to 60V, applied through the shunt resistor connected in series between the power supply and the load. The voltage source enters the specimen from Probe A and is expelled at the negative terminal of the power supply connected to Probe B. A TiePie HS6D differential oscilloscope was utilised to acquire and log the data of potential differences over the probe terminals at a 1kHz sample rate. The voltage was held constant for 1 second for each increment. In addition, the oscilloscope measures the acting current by capturing the voltage drop accross a shunt resistor.

The application of potential creates a uniform electric field in the width, w, but a possibly non-uniform across the thickness, t. In principle, the determination of the electrical conductivities in transverse and through-thickness directions, denoted as σ_x and σ_z, respectively, can be derived from the difference in the measured voltage at the top probe, V_t, and the measured voltage at the bottom probe, V_b due to the non-uniform current density across the cross-sectional area wxt within the probe distance, δ.

According to the previous study by Buser [5], the difference in the voltage probe readings becomes more apparent as the specimen thickness increases. He observed that the difference in voltage readings for $[0]_{8s}$ UD layup for Toray TC1200 and Solvay APC is negligible as $|V_t/V_b| < 2\%$. Hence, the $V = Vt = Vb$. However, when investigating the laminate with $[0]_{16s}$ and $[0]_{32s}$ UD layup, the difference is not negligible and, therefore, should be taken into account in the determination of σ_x and σ_z.

In the data analysis, the voltage and current were logged as an average over each second of the voltage increment. For each specimen, the measurement was performed twice by flipping the specimen with a 180° rotation along the specimen length for the second evaluation. By flipping the specimen, the average result of the conductivity obtained is more representative by reducing the most favourable conductive paths within the specimen, as depicted in Figure 3.3.

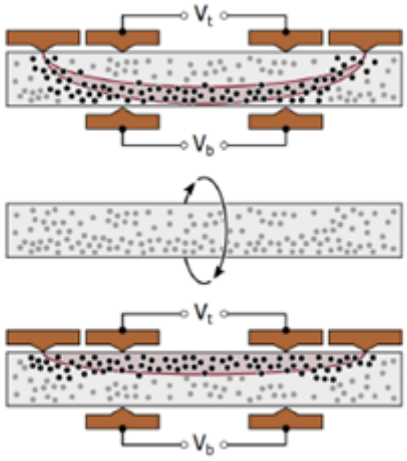

Figure 3.3. Rotating transverse sample to reduce the influence of preferred conductive path [3]

Determination of the electrical conductivities in the transverse direction, σ_x, and through-thickness direction, σ_z, has been approached by implementing a 2D numerical model in cases where $Vt > Vb$. The model was assembled in the COMSOL Multiphysics, which will be elaborated further in the next section.

3.2.2 Data Reduction for Six Probe Measurements (COMSOL Model)

The numerical model was implemented in COMSOL Multiphysics in order to determine the electrical conductivity in the transverse direction, σ_x, and through-thickness direction, σ_z. Buser [6] proposes a 2D xz-plane to iteratively solve for the anisotropic conductivities. The mesh created in COMSOL is polygonal and can be refined in the location where high current density gradients appear, such as at the point of current introduction. The mesh for the transverse specimen constructed in COMSOL is shown in Figure 3.4. Note that the half-model is implemented, instead of a full model, by applying a symmetric boundary condition around the xz-axis.

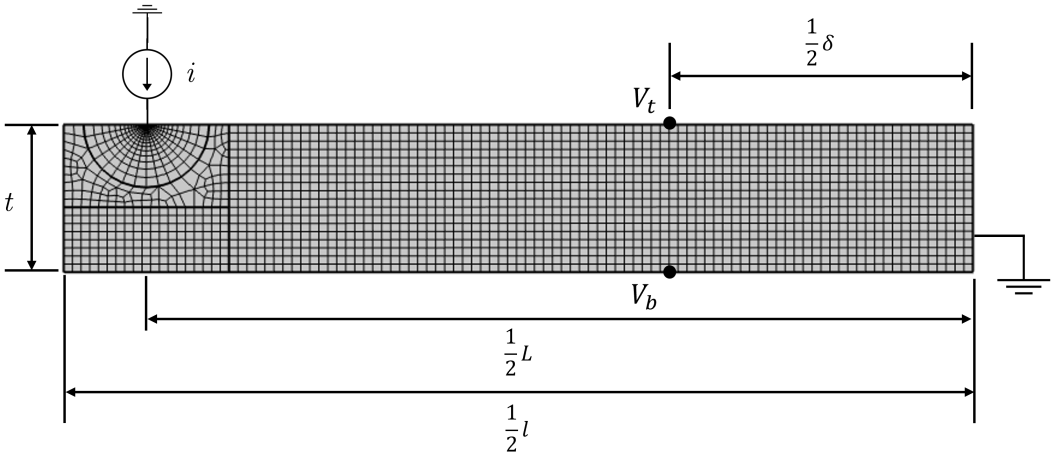

Figure 3.4. COMSOL mesh of the specimen for six-probe method [6]

The flowchart of the implementation of the numerical model in COMSOL Multiphysics is depicted in Figure 3.5. The numerical model numerically solved Ohm's Law for the current density, J, and

the electrical field, E, obtaining the nodal voltage, V, at every point. The solution of the nodal voltage is obtained by calculating the objective function, F, which is the absolute difference between the measure values of the top and bottom voltage and numerically calculated voltages of the voltage probe. The objective function, F, can be expressed as the following

$$F = \sqrt{(V_{top,exp} - V_{top,num})^2 + (V_{bot,exp} - V_{bot,num})^2} \tag{3.1}$$

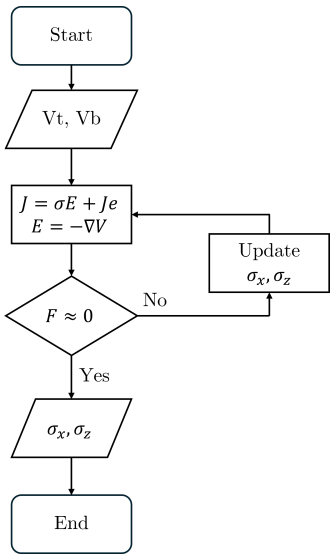

Figure 3.5. Flowchart of simulation process in COMSOL Multiphysics

Ohm's Law is numerically solved by iteratively calculating the objective function, F, until it is approximately equal to 0. If F is not satisfied yet, a new iteration is started with updated conductivity values, and the algorithm is looped until F is satisfied, at which point the conductivity values are obtained.

3.3 Micrograph Analysis

This section will provide the process of analysing the micrographs of the specimens. The procedure to analyse the microstructure of the material begins with preparing the specimen for microscopy, followed by the image analysis developed in this study. These procedures will be discussed in detail in the following subsections.

3.3.1 Specimen Preparation and Microscopy

The Keyence VHX 7000 Digital Microscope, available at the University of Twente, was utilised to capture a high resolution of the cross-section micrographs of the specimen that was previously characterised using the six-probe method.

A cross-section of the specimen perpendicular to the fibre direction was first cut with a diamond saw. The cut sample was then embedded in an epoxy resin. Embedding of the sample ensures that the sample has the proper fixation on the position with respect to the lens of the microscope. The embedded sample was then sanded and polished using the Struers Tegramin equipment for high-quality specimen preparation. Proper and careful grinding and polishing are of high importance to

ensure the high quality of surface finish and cross-section image, which will improve the accuracy of the subsequent image analysis. For each material, one cross-section micrograph was considered for developing the resistor network. The dimensions of the micrograph are approximately 12.000 x 3000 pixels, which is large enough to capture part of the specimen cross-section. An example of the cross-section micrograph for Toray and Solvay material is shown in Figure 3.6a and Figure 3.6b, respectively.

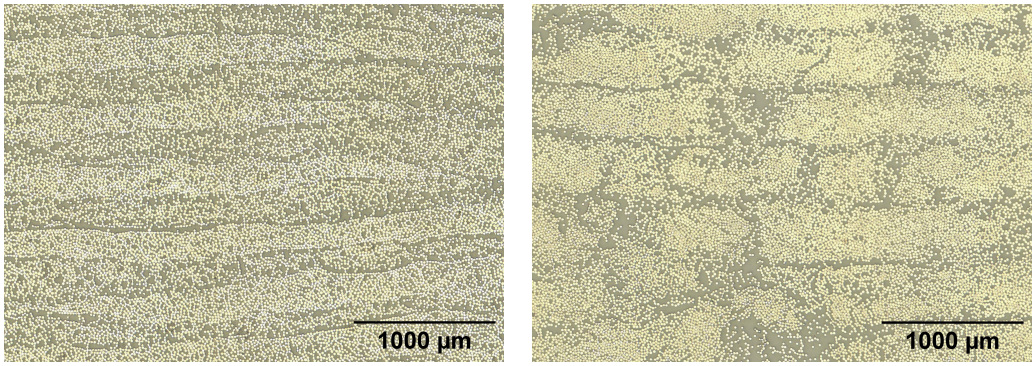

(a) Micrograph of Toray C/PEEK (b) Micrograph of Solvay C/PEKK

Figure 3.6. Micrographs of $[0]_{16s}$ consolidated laminate

3.3.2 Image Analysis

Cross-sectional micrographs were obtained from specimens of Toray TC1200 C/PEEK and Solvay APC C/PEEK materials, as illustrated in Figure 5.1. The specimens were embedded in Struers EpoFix resin and polished using a Struers Tegramin polishing machine. A total of 100 micrographs, each measuring 300 x 300 μm^2, were analysed for each material. This analysis aims to determine the coordinates of the fibre centres and the radius of each fibre. This analysis involves two main steps: detecting the fibre centres and determining the fibre radii.

The principal algorithm for detecting fibre centre coordinates is visualised in Figure 3.7. In this study, the Python library OpenCV was employed to determine fibre contours to create a circle that overlays the contour and extract the corresponding coordinate of the fibre centre.

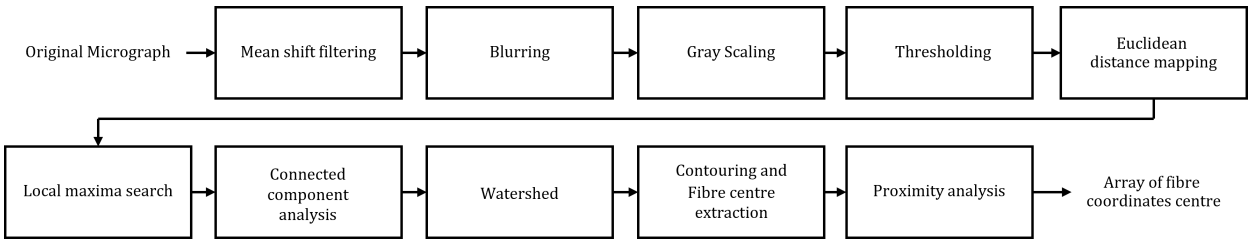

Figure 3.7. Step of image analysis of the procedure to extract fibre coordinate

Before implementing the contour algorithm, the images are pre-processed. Firstly, the fibres are separated from the background through mean-shift segmentation, illustrated in Figure 3.8b. This method adjusts the intensity of each pixel by comparing it to surrounding pixels based on the spatial window radius, S_r, and spatial colour radius, S_p. The segmentation process considers pixels that are spatially close and have color intensities within the specified ranges, which correspond to S_r and S_r, respectively. After the segmentation process, the image is blurred and converted to greyscale, as visualized in Figure 3.8c. Due to slight variations in lighting conditions across the length of large

micrographs, adaptive thresholding, specifically binary thresholding, combined with Otsu's method, is required. Otsu's thresholding assumes a bimodal distribution of pixel intensity in the image. Since the cross-section of composite materials typically comprises two distinct components—fibres and matrix, which exhibit two different colours—Otsu's thresholding is suitable for this analysis.

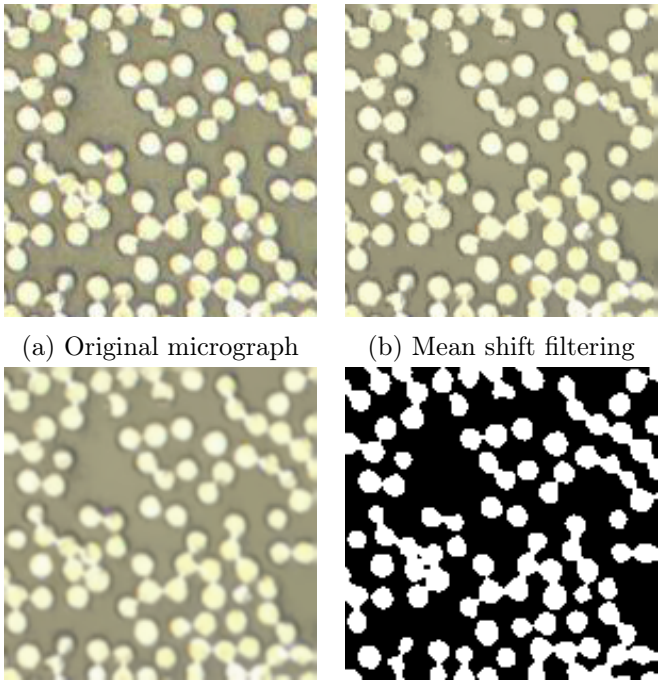

(a) Original micrograph (b) Mean shift filtering

(c) Blurring (d) Thresholding

Figure 3.8. Image analysis technique applied to obtain binary image from original micrographs

The binary image, shown in Figure 3.8d, is obtained after the thresholding step and is utilised to generate an Euclidean distance mapping matrix. A local maxima search is then conducted on the matrix to identify the points with the highest Euclidean distance values. However, these local maxima do not necessarily correspond directly to the fibre centres. In some cases, multiple neighbouring points within the matrix are identified as local maxima for a single fibre due to their equivalent Euclidean distances. The example of local maxima is presented in Figure 3.9a, where multiple maxima are found in one fibre due to the equivalent distance to the closest boundary between the fibre and the matrix. To accurately determine the fibre centres, fibre contours are analyzed using the local maxima matrix in combination with the watershed algorithm.

Due to the high packing density of the fibres, extracting individual fibre coordinates from a binary image after thresholding is challenging. In line with the approach in [23] on composite micrographs, the watershed algorithm is employed to differentiate between connected fibre contours. The topological 8-connectivity watershed algorithm [24] was implemented to separate multiple fibres. After the algorithm was implemented, each fibre was identified by one contour, as shown in Figure 3.9b. Subsequently, an overlaying circle is drawn from each contour to determine the corresponding centre coordinate and radius. The final step involves proximity analysis, where fibre centres closer than the specified minimum fibre radius, R_{min}, are merged into a single fibre centre. The result of the extraction of the fibre centre coordinate and the corresponding fibre segmentation obtained from the contour analysis are shown in Figure 3.9c and Figure 3.9d, respectively.

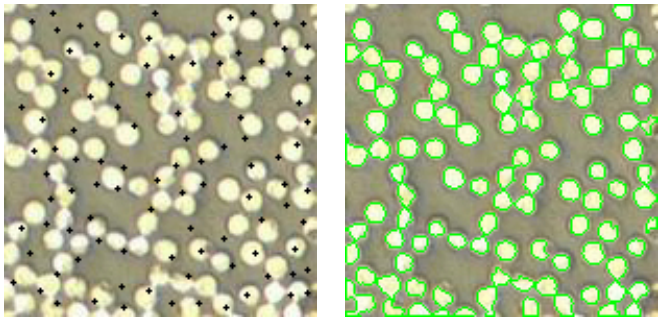

(a) Local maxima based on Euclidean distance

(b) Fibre contour after implementing watershed

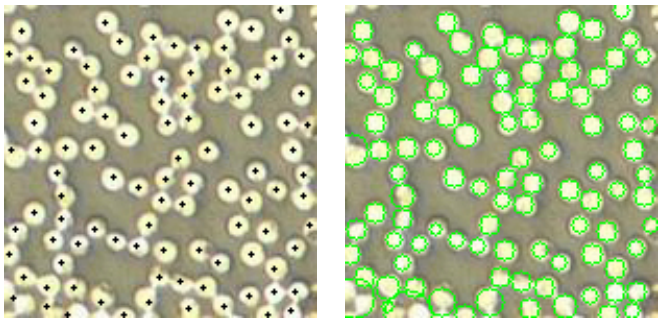

(c) Fibre centre points from contour analysis

(d) Segmentation of fibre from contour analysis

Figure 3.9. Image analysis technique applied to obtain fibre segmentation from binary image

The subsequent step in the image analysis is the fibre radius calculation. Initially, the fibre radii were determined based on the defined contours implemented using the function in SciPy. This approach often leads to inaccuracies because the contour method essentially defines the radius from the minimum enclosing circle, which completely covers the contours with minimum area. This can result in over- or underestimating the fibre radius. In another case, after the proximity analysis, where closely spaced centre points are merged, the radius calculated based on the contour would be very large, which does not represent the fibre in general. This phenomenon can be seen in Figure 3.9d where a few fibres show a smaller green circle than their actual size, as well as a bigger circle that covers more than one fibre in the lower boundary area.

An algorithm of fibre radius search was implemented to calculate the fibre radius based on the grayscale value of the centre pixel to improve accuracy. This method, previously employed by Katuin in his research [25], allows for a more precise determination of the fibre radius. The flowchart illustrating this fibre radius calculation process is presented in Figure 3.10.

Firstly, the centre points obtained from the proximity analysis are used as input for this section of the algorithm. A fibre radius function is applied in four directions—left, right, top, and bottom—to determine the radius in each direction and then calculate the average fibre radius.

In this radius calculation function, the grayscale value of the centre pixel serves as the main variable, while the grayscale value offset, Δ_{GV} determines whether a pixel is considered part of the fibre, as visualized in Figure 3.11. The value of Δ_{GV} is derived from the difference in pixel intensity between the fibre and the matrix, as seen in the image histogram. This offset is subtracted from the grayscale intensity of the centre pixel, as shown in the left block of Figure 3.10, allowing for a more precise determination of the fibre radius.

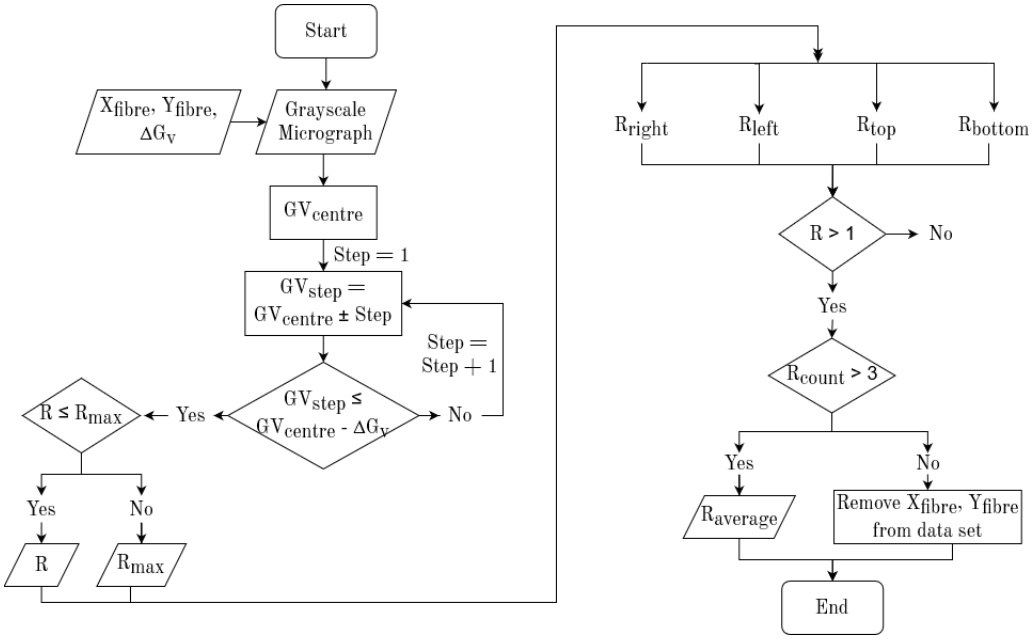

Figure 3.10. Flow diagram of the procedure to calculate fibre radii

Before calculating the average fibre radius, R_{avg}, the found radii are checked using criteria that specify a minimum of three radii found having a minimum of one pixel. The average fibre radius is then compared with a specified minimum fibre radius, R_{min}. If the detected fibre radius does not meet these two conditions, the detection is considered erroneous and excluded from the dataset. During the process of finding the fibre radii in different directions, the observed radius R is compared with a specified maximum radius, R_{max}. According to the manufacturer, the typical AS4 and ASD4 fibres have an average diameter of 6.7-7.1μm [26]. Therefore, to account for tolerance in error in the fibre search algorithm, R_{max} is set to 4μm for this analysis. The specified maximum radius, R_{max} is chosen instead if any of the detected R for a fibre in one direction exceeds this R_{max} value. The steps of the calculation of R_{avg} are presented in the right block of the flow diagram. The result of the fibre radius calculation using the fibre radius search algorithm is presented in Figure 3.12. In addition, the values of parameters used in the image analysis process are summarized in Table 3.2.

Material	Toray TC1200	Solvay APC
Ratio (pixel/μm)	1.678	1.679
Ratio (μm/pixel)	0.596	0.596
Image Settings		
Spatial window radius, S_p	20	20
Spatial window colour, S_r	10	10
blurkernel	1	1
GrayOffset, Δ_{GV}	80	60
Maximum radius, R_{max}	4	4
Minimun radius, R_{min}	2	2

Table 3.2. Parameters used for image analysis

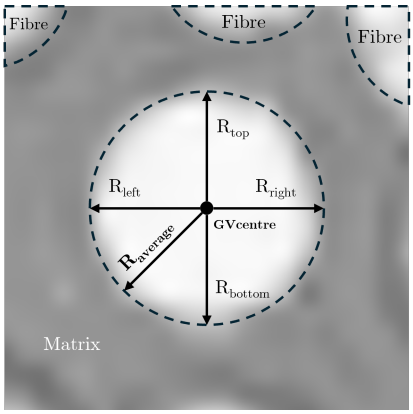

Figure 3.11. Fibre radius determination in four directions

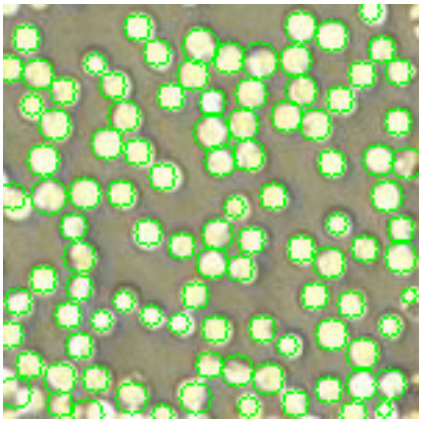

Figure 3.12. Fibre segmentation after implementing the fibre radius search algorithm

3.3.3 Voronoi Tessellation

The construction of the Voronoi pattern can be described as dividing a 2D plane into areas that are called Voronoi polygons or Voronoi cells. Each cell is assigned to a given input point in a plane, in this case, the coordinates of each fibre inside the cross-section, and occupies a region around the point. The unique characteristic of a Voronoi tessellation is that any randomly selected point in one particular cell is closest to the corresponding input point [27]. The Voronoi tessellation cell is illustrated in Figure 3.13.

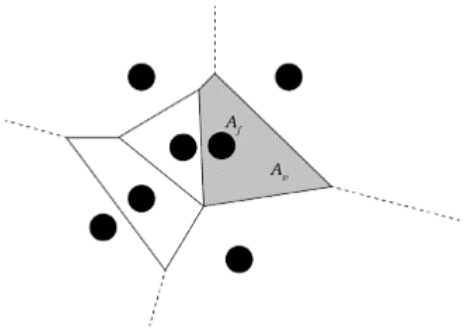

Figure 3.13. Voronoi tessellation surrounding fibre centres [25]

According to the characteristics of Voronoi tessellation, the points located at the outermost boundary have an infinite area size of a Voronoi cell and cannot be included in the analysis. This makes it impossible to analyse the fibre volume fraction at the edges of the micrograph. To circumvent this, the Voronoi cells at the outermost points are finitize and subsequently intersected with the tape surface edges to create a finite Voronoi tessellation, as schematically shown in Figure 3.14b.

In principal, the finitization of Voronoi cell is performed by creating new finite points that construct Voronoi cells for the cells located on the edge of the micrograph. Subsequently, combining the boundary points of the edges of the micrograph yields a finite Voronoi cell that corresponds to the micrograph boundary fibres.The detail elaboration of the process of finitizing the Voronoi cell can be found in Appendix A

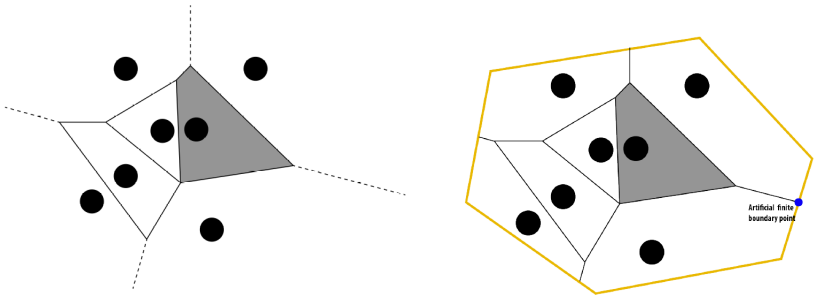

(a) Voronoi cell with infinite boundary element

(b) Voronoi cell with finite user-defined boundary element

Figure 3.14. Voronoi tessellation [25]

The final step in a finitization algorithm is to import the boundary points that correspond to the boundary points of the edges of the micrograph. This study used specified square window sizes, and therefore, the boundary points defined were four points that correspond to each corner in the micrograph. Figure 3.15 shows a micrograph of the Toray specimen with a boundary polygon defined. The Voronoi ridges, which are finitised from the aforementioned step, are intersected with the imported boundary polygons. The Shapely library in Python was used to determine whether a Voronoi ridge intersects with a boundary polygon. If there is an intersection between the modified Voronoi ridge and the boundary, the ridges are modified the second time to create a closed cells that correspond to the micrograph boundary. If there is no intersection, the Voronoi ridges remain the same.

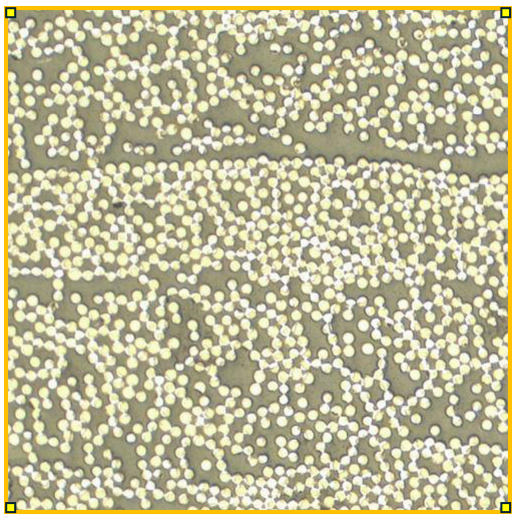

Figure 3.15. Micrograph with boundary polygon at the edges

The area of the Voronoi cells is defined using the ConvexHull function from the SciPy spatial library in Python. By knowing the area of the Voronoi cell, A_v, the fibre diameter, d_f, and consequently the fibre area, A_f, one can calculate the local fibre volume fraction based on the Voronoi tessellation, V_f, which can be expressed as the following

$$V_f = \frac{A_f}{A_v}. \tag{3.2}$$

With the Voronoi tessellation, identified fibre centre coordinate, and identified fibre radius, the Voronoi cells and the local fibre volume fraction, V_f, can be analysed for each RVE. A Voronoi diagram, including a V_f colour plot of a Toray sample, is provided in Figure 3.16. Each Voronoi cell is filled with a colour based on the V_f value, ranging from 0 to 1. A V_f of 0 means that the Voronoi cell is infinite, whereas a V_f of 1 indicates that the area of the Voronoi cell is equivalent to the fibre area. By analysing this image, it can be seen that the fibre and resin are not homogeneously distributed within the tape. The fibre cluster is visualised with a V_f value close or equal to 1, and the region of the resin-rich interlayer is indicated with a lower V_f with a value ranging from 0.1 to 0.3. The variation in V_f of each Voronoi cell is further analysed to define the fibre interaction and subsequently generate a Voronoi tessellation-based resistor network for each RVE.

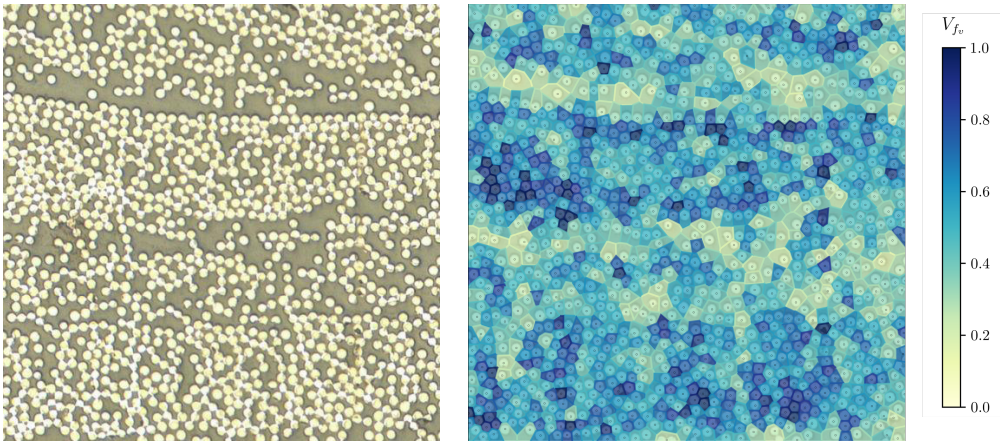

(a) 2D cross-section micrograph

(b) Voronoi cell distribution within the micrograph

Figure 3.16. Voronoi cells with V_f colour plot from the 2D cross-section micrograph

Chapter 4

Modelling

In this chapter, the modelling of the spatial statistics and the quasi-3D resistor network are discussed in detail. Section 4.1 explains the determination of representative volume elements used in the model. Section 4.2 describes the process of analysing the fibre distribution in the micrograph by implementing 2D statistical descriptors. Lastly, the description of generating the quasi-3D network model is presented in Section 4.3.

4.1 Representative Volume Element (RVE) Determination

Representative volume elements (RVE) is an important concept when analysing a heterogeneous material for a homogenisation problem. In principle, RVE is an image of a sub-region in which the average properties values are similar or can represent the entire bulk material. It is considered an important parameter, especially when modelling the material, where the smallest microstructural window size can reduce computational time.

Trias [28] estimated the RVE size for different criteria to be 50 times the radius of the fibre. There are many suggestions of the RVE size that were found in the literature, but in principle, the consideration of determining the proper RVE size depends highly on the associated properties that are being investigated. In this current work, the fibre distribution in the cross-section plays a vital role in modelling the resistor network based on the specimen microstructure. Therefore, the parameters that were considered were the fibre density, the fibre volume fraction based on a micrograph, and the fibre volume fraction based on Voronoi analysis.

The method employed in determining the window size is based on a one-way analysis of variance (ANOVA), which is a classic statistical analysis used to compare the means and variance of dependent variables across multiple groups. The idea is to determine if there are any statistically significant differences between the aforementioned parameters (dependent variables). The ANOVA analysis was performed in increasing window size (independent variable), ranging from 100 μm to 500μm, as illustrated in Figure 4.1. For each window size, ten micrographs were analysed using one-way ANOVA. A more detailed calculation is provided in Appendix C.

The null hypothesis (H_o) used in this analysis is that there is no statistical significance between groups for the examined parameters. For the calculation, the α represents the threshold for rejecting the null hypothesis when compared with the calculated P-value that describes the probability that the observed differences in group means occurred by chance. In this analysis α is chosen to be 0.05.

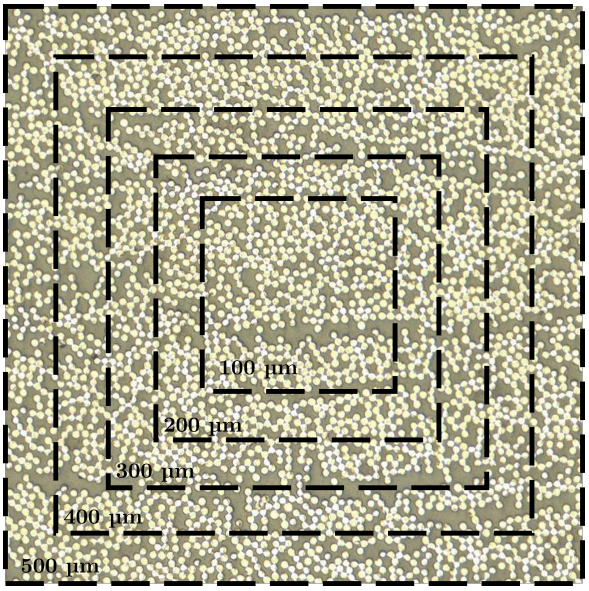

Figure 4.1. Increasing RVE sizes ranging from 100 to 500μm

The result, provided in C, shows that the P-values were found to be higher than 0.05, meaning that it fails to reject the null hypothesis. This result suggests a statistical insignificance for each parameter with increasing window sizes, meaning that selecting any window size can be considered statistically representative.

Although the analysis yielded a statistically insignificant result, some parameters need to be considered in terms of practical and physical relevance. For instance, a small window size, i.e. 100μm, might not be able to capture the inherent variability in the specimen microstructure. The variability includes the fibre distribution in the inter-laminar region, which is important in investigating the through-thickness conductivity. On the other hand, a large window size, i.e. 500μm, while it can capture higher amounts of fibre and is more representative of the bulk material, increases the complexity of fibre interaction, leading to potential computational inefficiency. Hence, it was decided to select a 300μm window size, which is deemed statistically representative, maintains a practical and physically relevant scale for modelling, and avoids potential challenges when using too small or too large window size.

4.2 Nearest Neighbour Analysis

Cross-sectional micrographs obtained from Toray TC1200 and Solvay APC specimens with the dimension of 300x300 μm^2 were statistically analysed. As previously mentioned in Section 2.2, four statistical descriptors are used to quantify the short and long-range interaction of fibres, such as nearest neighbour distance, nearest neighbour orientation, Ripley's K Function, and pair distribution function. The principal steps for quantitatively assessing the statistical spatial distribution of the fibre are visualised in Figure 4.2 and elaborated in more detail in the following subsections.

4.2.1 Nearest Neighbour Analysis

The analysis of the nearest neighbour distance starts by identifying the closest neighbour for each reference fibre present in the micrograph. This can be done by using the SciPy spatial library with

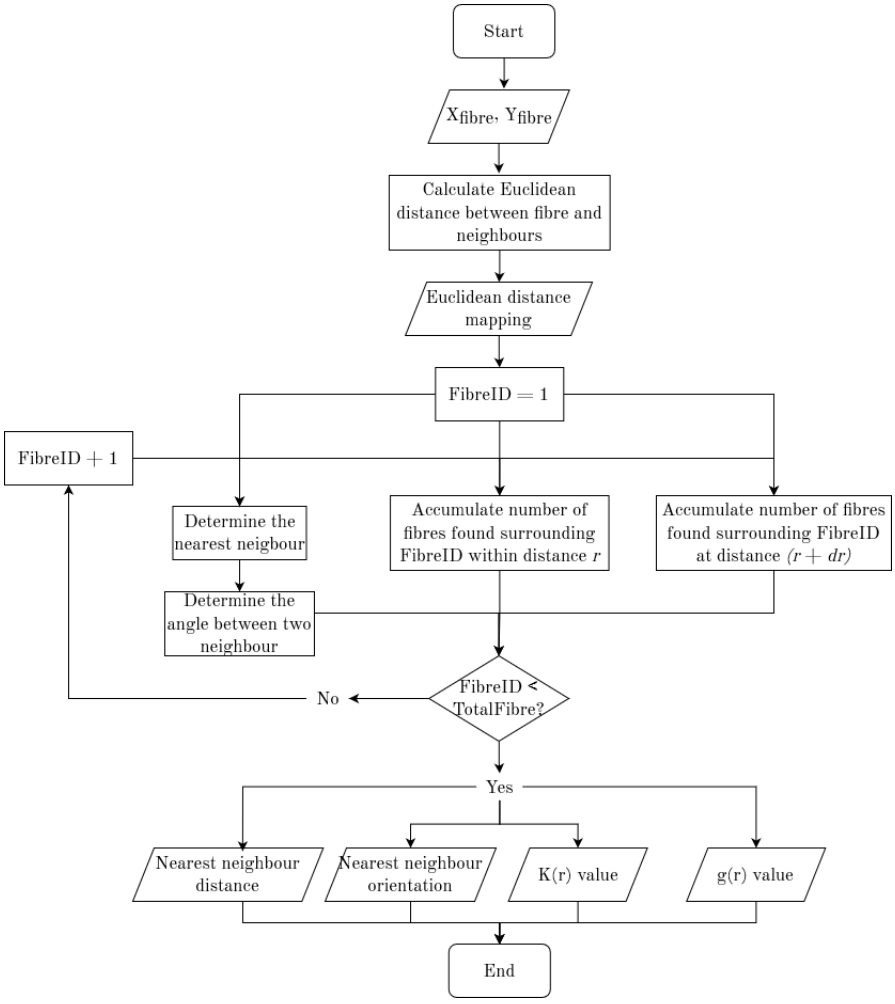

Figure 4.2. Flowchart of nearest neighbour analysis

the cKDTree function to do a quick search of the nearest neighbouring points. Once the nearest neighbour of the fibre is determined, the Euclidean distance between them is measured. These distances are then compiled into a distribution, providing insights into the arrangement of fibre in short to medium ranges. A high concentration in short nearest-neighbour distances might indicate clustering, whereas a wider spread of distances suggests a more dispersed or random distribution of fibres.

4.2.2 Nearest Neighbour Orientation

The analysis of nearest neighbour orientation begins with a similar step to the analysis of nearest neighbour distance. The process starts by identifying the first nearest neighbour location of the reference fibre. Once the nearest neighbour is determined, the angle between the line connecting two fibres is measured with respect to the horizontal axis. This process is repeated for all fibres in the micrograph. The resulting angular data is plotted as the cumulative distribution function and compared with the CSR diagonal line, indicating a completely random distribution of fibres. By analysing this orientation distribution, one can detect whether there might be a preferential direction in the fibre arrangement. The analysis helps determine whether the fibres are randomly distributed or exhibit some degree of alignment, which might be of importance in composite materials where directional properties are critical.

4.2.3 Ripley's K Function

Analysing the spatial distribution using Ripley's K Function starts by selecting a reference fibre and measuring the Euclidean distance to the surrounding fibres. The number of fibres in the surrounding area that is located within the specified radius from the reference is counted. Subsequently, the edge correction is conducted by calculating the ratio of the circumference of the circle radius within the RVE to the whole circumference. This process is then followed by accumulating the number of fibres found within the particular radius for every reference fibre in the micrograph. This count is repeated for increasing radii, which effectively evaluates how the spatial distribution of fibres changes over different distances. The counts are then compared to the expected counts from a CSR pattern to assess whether the fibres are more clustered or more regularly spaced than expected by chance. If the observed counts, or K value, exceed the CSR curve, it indicates clustering at that scale, while lower values suggest regularity or dispersion.

4.2.4 Pair Distrbution Function

The analysis begins with calculating the Euclidean distances between reference fibres and all of the fibres in the micrograph. For each distance, r and the outer radius, $r + dr$, the possibility of finding a fibre at that annular region relative to a reference fibre is measured and compared to what would be expected for a completely spatially random (CSR) pattern. This measurement is repeated for every fibre in the micrograph and the increasing distance r. The outer radius, $r + dr$, in this analysis is chosen to be constant with the value of 0.5 μm.

4.3 Quasi-3D Resistor Network

The extracted fibre coordinates and the fibre radius from Section 3.3.2 are further analysed in this section. The aim of this section is to generate a graph network based on the Voronoi tessellation using fibre centre location and radius that were extracted from the image analysis. The Voronoi tessellation, also known as the Dirichlet region, together with the inter-fibre distance, is considered to define the interaction between a reference fibre and its surroundings. The proposed resistor network model is implemented using Python. The procedure to generate a resistor network model consists of the following steps:

1. Create a Voronoi tessellation and the corresponding local fibre volume fraction, V_f, for each Voronoi cell. The output is an array that stores the coordinates of the fibre centre, the fibre radius, and the particular V_f for each fibre.

2. Create fibre connectivity of fibre interaction based on interfibre distance and local fibre volume fraction. For each connection, calculate the resistance ($2\rho L/A$), where ρ is the fibre conductivity, L is the length of the contact point, and A is the cross-sectional fibre area. The output is a graph network comprising nodes and edges representing the fibre-to-fibre contact in a 2D cross-section with calculated conductance value between the contacting fibre.

3. Formulate the resistor network in matrix form based on the graph nodes and edges and boundary conditions considered for transverse and through-thickness directions.

4. Solve for nodal voltage and current using Kirchoff's Current Law and calculate the equivalent resistance.

4.3.1 Inter-fibre Interaction

As previously mentioned in Chapter 1, in the transverse and through-thickness directions, the current flow is heavily influenced by the occurrence of fibre-to-fibre contacts caused by morphological occurrences in the fibre direction, such as fibre clustering and waviness. Resulting in low conductivity in both directions compared to the conductivity in the fibre direction due to the limited number of contact incidences in both directions.

Hong Yu [20] predicted the electrical conductivity of a UD single-layer CFRP by formulating a 3D resistor network model. The generation of the 3D network was based on the 2D cross-sectional micrograph using an inter-fibre spacing to define the connectivity, as shown in Figure 4.3a. The micrograph was extended in the fibre direction to create the overall network. The contact points in the fibre direction were defined by taking the fibre waviness parameter into account to determine the length between contact points, L. These contact points were randomly located to mimic the stochastic nature of fibre-to-fibre contact. The fibre and contact resistances are then transformed into a resistor network spanning over the longitudinal and transversal direction, as depicted in Figure 4.3b (the model is only depicted in the longitudinal direction in the figure). The model resulted in a good agreement with the experimental data. However, the model was limited to only accounts for a single ply without a significantly resin-rich layer.

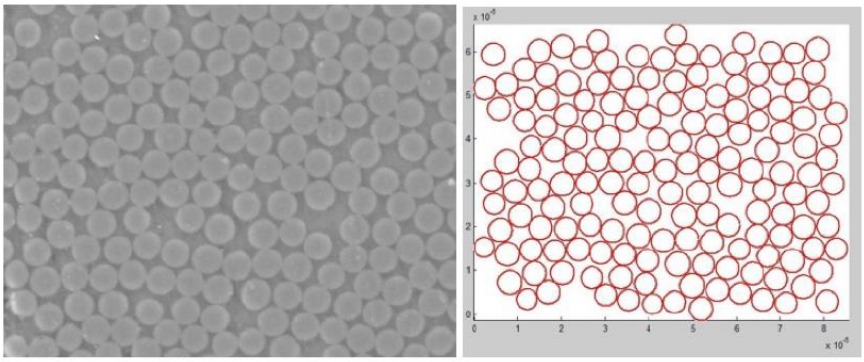

(a) Schematic of 2D cross-sectional UD composite micrograph

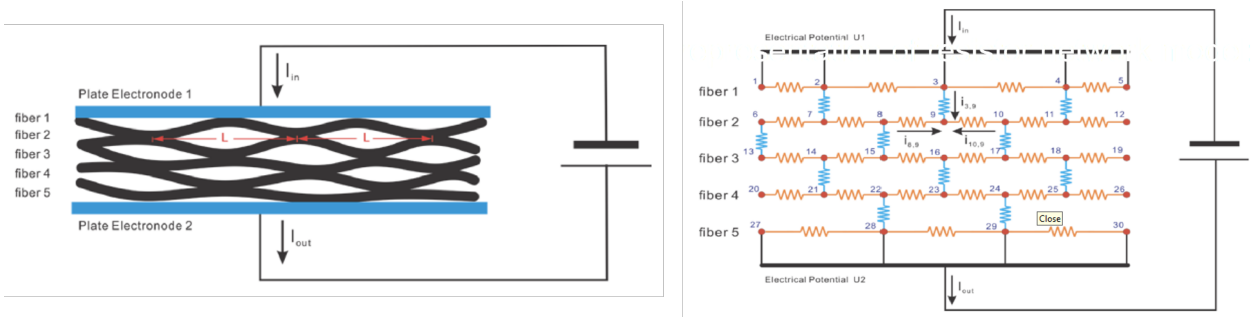

(b) Schematic diagram of fibre resistor network model. For clarity, only 2D model is presented

Figure 4.3. 3D resistor network model obtained from micrograph and extended to the fibre direction [20]

Looking into the 3D resistor network model from [20], this current work considered the resistor network model from the 2D cross-sectional micrograph, which also takes into account the interlaminar resin-rich region. From the known fibre centre location that was previously obtained from the image analysis, each fibre is extended in the fibre direction and contacts its neighbours at one contact point. This method generates what is called a quasi-3D resistor network model. The

purpose of using only one contact point is to reduce the computational cost while also enabling the calculation of a hundred resistor networks for each material. This model takes into account all the fibre distribution within the micrograph, including where there is a resin-rich interlayer region. The quasi-3D model with one contacting point, denoted with a red star-shape, is visualised in Figure 4.4.

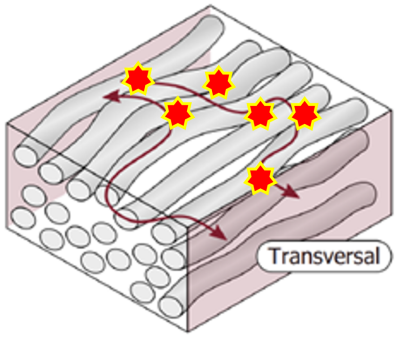

Figure 4.4. Schematic of one contact point between fibre in fibre direction, denoted with red dot

In this resistor network model, the interaction of fibres is determined using a percolation threshold approach. The percolation threshold refers to the point at which enough fibres are sufficiently close to form a continuous conductive network. The schematic of the percolation threshold approach is visualized in Figure 4.5. When the reference fibres and their neighbour (denoted with red circle and yellow cells, respectively) are in direct contact, they create conductive paths independent of the matrix conductivity. However, in regions where fibres are not directly in contact, the neighbouring fibre could be in close proximity, in which the matrix or resin-rich areas might contribute to the conductive path. Threshold values are applied to both the local fibre volume fraction, V_f, and the inter-fibre distance, d, between a reference fibre and its neighbours.

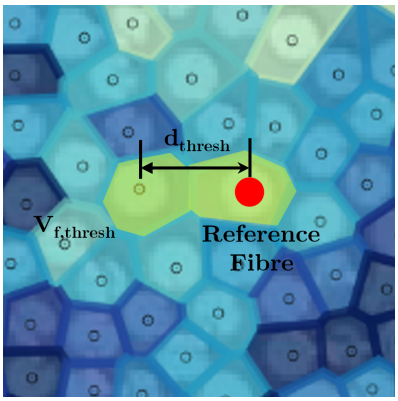

Figure 4.5. Schematic of implementing threshold values for reference fibre and its neighbour

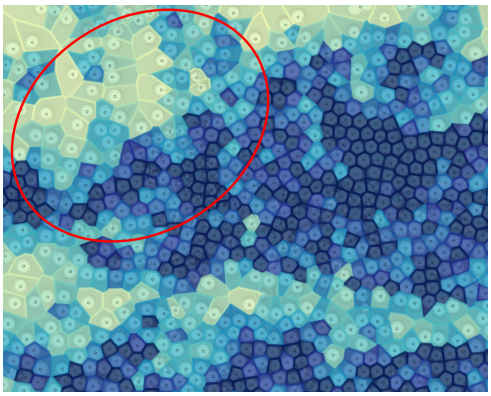

Figure 4.6. Voronoi cells at boundary having low V_f value but yet still spatially close with its adjacent fibres, indicated with red ellips

During the generation of the model, fibre connectivity is defined using the threshold value for fibre spacing, d_{thresh}, and the local fibre volume fraction, $V_{f,thresh}$. d_{thresh} reflects the maximum allowable distance between fibres to maintain electrical contact. This also represents the limit beyond which the local waviness causes fibres to be too far apart to maintain electrical connectivity. Furthermore, $V_{f,thresh}$ determines the critical fraction of fibres required in a local region to maintain conduction

paths within the microstructure. Essentially, it indicates how efficiently the fibres are distributed. In addition, $V_{f,thresh}$ defines the boundary between a region with sufficient fibre to form a conductive path and where resin predominates, which hinders connectivity. The implementation of these two threshold values is used to account particularly for the nodes or the fibre that is in the boundary of the RVE in which the fibre might be close to a resin-rich region, where the V_f is large, but still spatially close to the surrounding fibre (visualised in Figure 4.6). The determination of these values was considered iteratively.

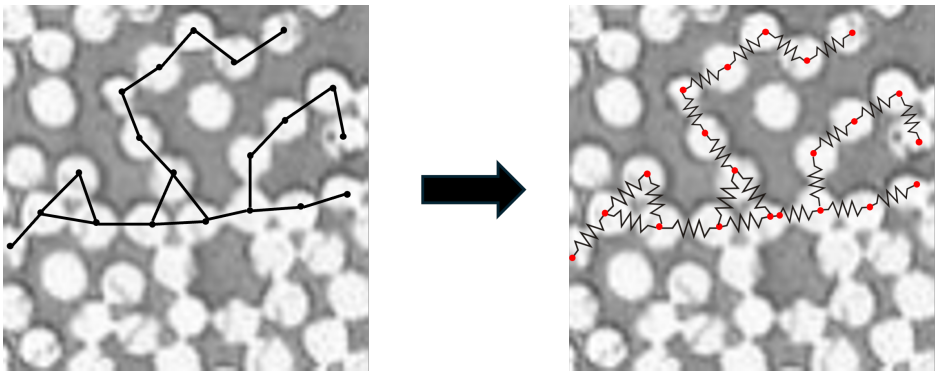

Figure 4.7. The fibre connectivity represented as connecting line transformed into 2D representation of quasi-3D resistor model

The fibre connectivity in the model is presented as a connecting line (also known as the edge in the network) between two centres of neighbouring fibres. In the quasi-3D resistor model, this represents the total resistance between two connecting fibres, whereas the connecting line is depicted as a resistor connecting the two fibre centres, as visualized in Figure 4.7. Furthermore, the resistance between two contacting fibres can be calculated by treating the fibre as a resistor and subsequently adding those two resistors in series, as depicted in Figure 4.8.

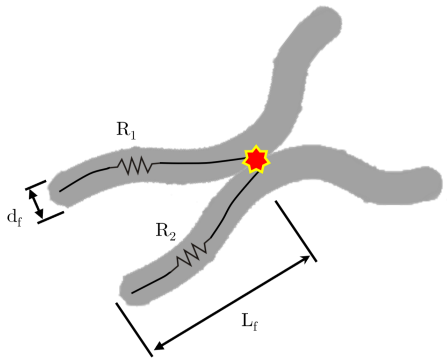

Figure 4.8. Schematic of the two fibres contacting at one point and how the total resistance is calculated

By looking at the schematic in Figure 4.8, the total resistance between two contacting fibres, represented by a weighted edge in the graph network, is calculated by using the following formula

$$R_f = \rho_f \frac{L_f}{\frac{\pi}{4} d_f^2}, \tag{4.1}$$

$$R_c = R_1 + R_2, \tag{4.2}$$

where ρ_f is the fibre resistivity, L_f is the contact length, and A_f is the cross-section area of reference fibre, R_c is the resistance between two contacting fibres, R_1 is the resistance of the first fibre, and R_2 is the resistance of the second fibre. In addition, the resistance between the two surfaces of contacting fibre is neglected in this calculation. ρ that is used in this calculation are $\rho_t = 2.611\text{x}10^{-5}$ for Toray material and $\rho_s = 2.710\text{x}10^{-}5$ for Solvay material [6]. The absolute value of the contact length, L_f, is defined using the normal distribution with mean $\mu = 0\mu$m and standard deviation $\sigma = 1\mu$m to simulate the stochastic nature of fibre-to-fibre contacting length. The value of L_f differs for every calculation of the resistor network model in different micrographs and threshold values considered. The calculated total resistance of one connectivity, R_c is then used as an input in the graph and later used to calculate the overall equivalent resistance. An example of the generated network in 2D is visualised in Figure 4.9.

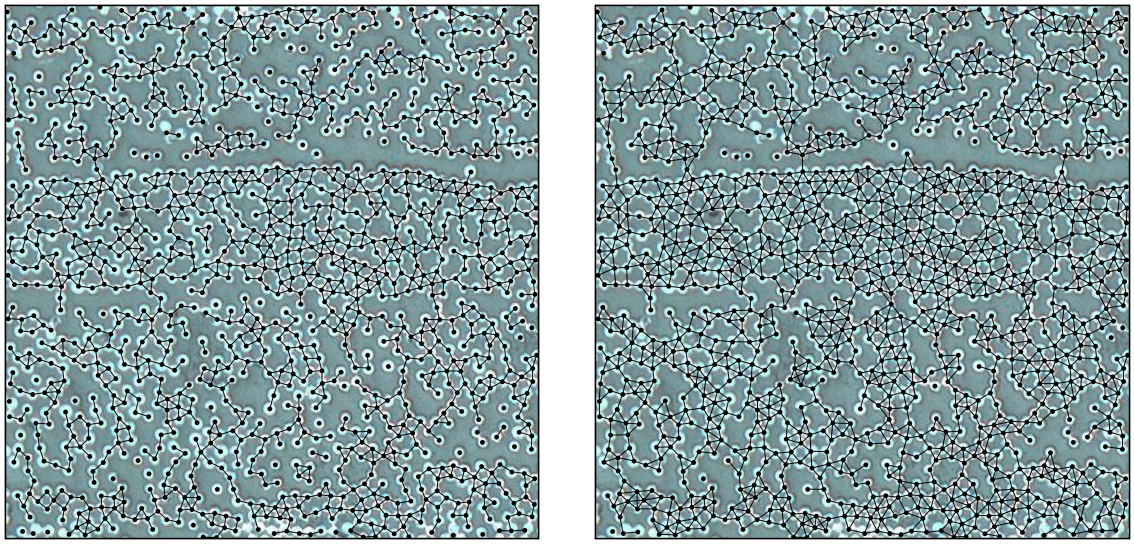

(a) Graph network with $V_{f,thresh} = 0.25$, $d_{thresh} = 8\mu$m

(b) Graph network with $V_{f,thresh} = 0.25$, $d_{thresh} = 10\mu$m

Figure 4.9. Examples of generated graph network

Figure 4.9a shows the graph network with $d_{thresh} = 8\mu$m and $V_{f,thresh} = 0.25$, and Figure 4.9b shows the graph network with $d_{thresh} = 10\mu$m and $V_{f,thresh} = 0.25$. As can be clearly seen in the figure, the lower d_{thresh} value results in less connectivity within the fibre in which no significant fibre clusters are present. Leading to fewer connected components in the overall graph network, whereas a higher d_{thresh} value creates bigger main connected components in the network. Furthermore, this value also affects the increase of the connectivity of the fibre in the through-thickness direction, which can reflect the lower equivalent resistance in a particular direction.

4.3.2 Boundary Condition

The graph network shown in Figure 4.9 is a 2D network that represents a quasi-3D resistor network with a defined resistance value for each connectivity. In order to evaluate the equivalent resistance in both transverse and through-thickness conductivity, nodes that represent the electrode in which the current source is applied are implemented and referred to as probe nodes, depicted as red nodes

in Figure 4.11. This approach similarly models the resistance measurement performed using the two-probe method [4]. For transverse direction, the nodes are applied on the left and right of the network, representing the source node and ground node, respectively. Meanwhile, the top and bottom nodes, which refer to the source and ground nodes, are added for the through-thickness direction. The source node is applied with the source current that was set to 1A, while the ground node was set to be -1A.

The probe nodes are then connected to the boundary points, or in this case, boundary fibres, that are located at the outermost within a micrograph. The determination of these boundary fibres is done by making use of ConcaveHull and alphashape function in Python [29]. Alphashape is utilised to generalize bounding polygons containing sets of points. It is used in computational geometry to describe the shape of a set of points, especially when it requires to capture the shape of the boundary points more accurately than a ConvexHull would, which may have missed a concave boundary.

The alphashape is controlled by a parameter α. The parameter α for creating a concave hull is determined iteratively by the alphashape function to obtain the best shape fit. Depending on the value of α, the resulting shape can vary between a convex hull for large values of α. And a more detailed shape that captures concave boundaries for smaller values of α. After several iterations in the program, it is found that the best fit for the α is equal to 0.03. The points that construct the concave hull are then obtained and separated according to the location and later will be used as boundary points for the calculation of equivalent resistance according to specified directions. Figure 4.10a depicts the constructed concave hull with the corresponding α value, indicated with a green line, and Figure 4.10b shows the specified boundary points with top, bottom, left, and right boundary points are indicated with green, orange, red, and blue nodes, respectively.

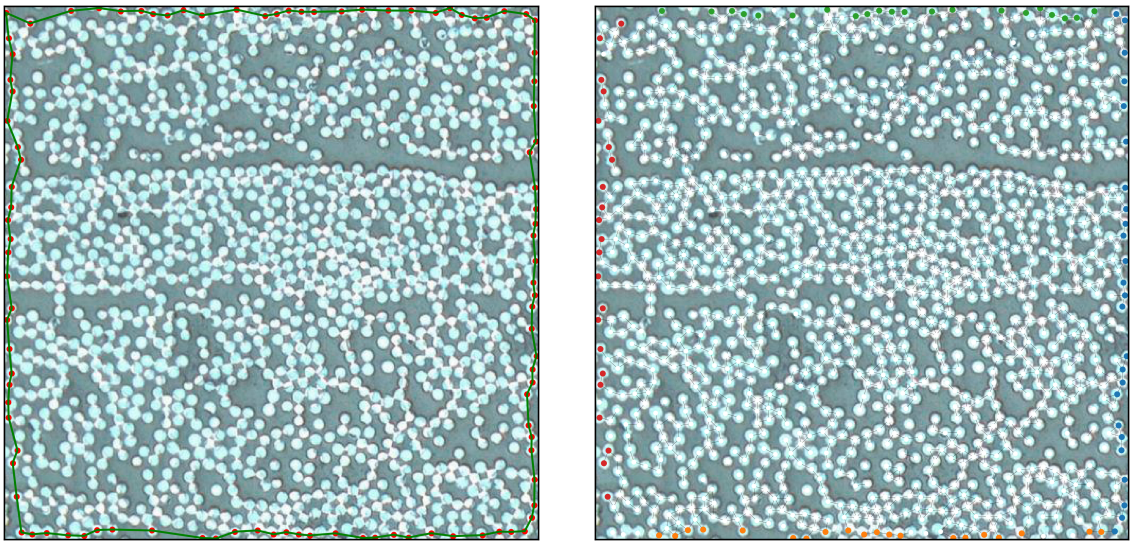

(a) ConcaveHull with $\alpha = 0.03$ (b) Boundary points obtained from ConcaveHull

Figure 4.10. The determination of boundary points from ConcaveHull and alphashape function in Python

Before evaluating the equivalent resistance, it is important to consider that there is a probability of fibre that is not connected to the main network due to the definition of the threshold value. The main network refers to the group of fibres connected to each other and where at least one fibre is connected to the boundary points. This network was also referred to as the conductive path from the source to the ground node. In case there is no connection between the fibre and boundary

points, the system of linear equations for solving nodal voltage will not have independent equations, resulting in a singular matrix that is not solvable. Therefore, the connected components need to be sorted to obtain the largest connected network before generating the conductance matrix $[G_N]$. In this way, the conductance matrix is guaranteed to be nonsingular, and the matrix operation, written in Equation 2.9 can be solved. An example of the largest connected component of the graph network is illustrated in Figure 4.11. The edges between the source and ground node and the boundary conditions were determined using the Equation 4.1 and 4.2 with the probe is treated as a fibre with $d_f = 7$ μm, $L_f = 10^{-6}$ μm, and ρ depends on the particular material.

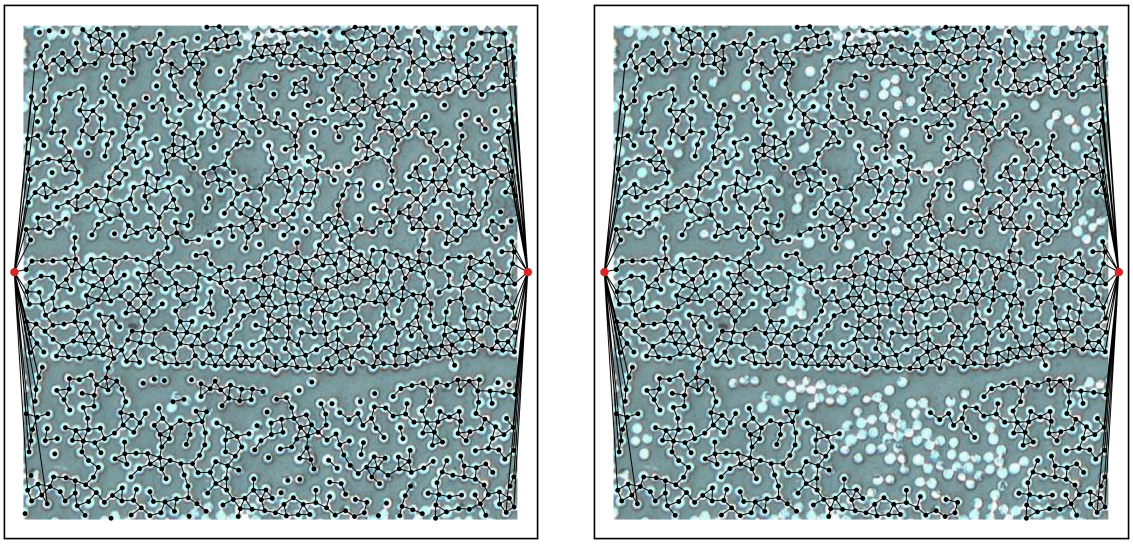

(a) Before the removal of unconnected components

(b) After the removal of unconnected components

Figure 4.11. Examples of generated graph network with boundary points, acting as electrodes

Chapter 5

Results

In this chapter, the results obtained from the experimental work and modelling in this study are presented. Section 5.1 provides the findings from the experimental work, including micrographs and the characterisation of conductivity using the six-probe method. Section 5.2 describes the fiber radius measurements obtained from the image analysis technique applied to the micrographs. Section 5.4 presents the statistical evaluation of the nearest neighbour distances within the micrographs. Finally, Section 5.4 provideees the results of the equivalent resistance calculations based on the quasi-3D resistor model.

5.1 Experimental Result

The cross-sectional micrograph of the specimen perpendicular to the fibre direction has been obtained through the microscopy procedure. A stitched micrograph of the specimen morphology from two similar lay-ups for Toray and Solvay material is shown in Figure 5.1a and Figure 5.1b, respectively.

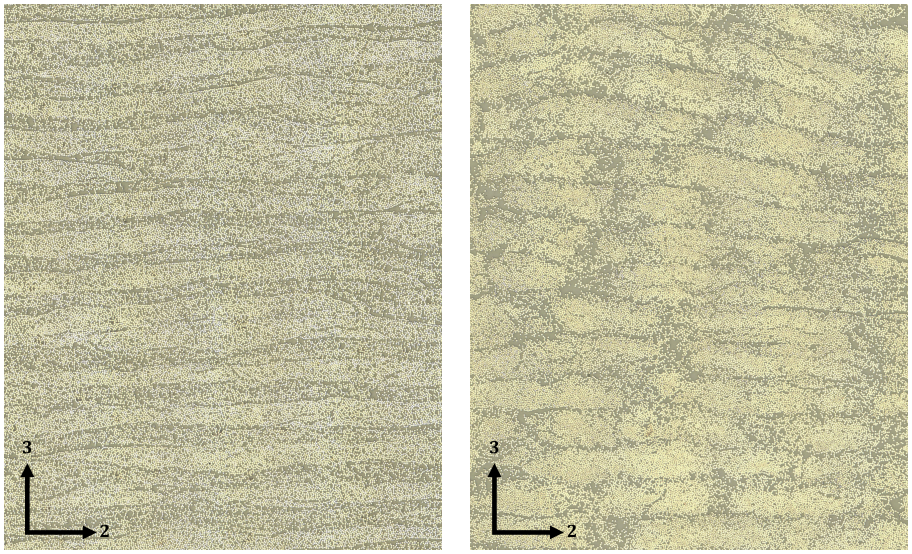

(a) Toray TC1200 (b) Solvay APC

Figure 5.1. Stitched Micrograph of $[0]_{16s}$ of consolidated specimens

5.1.1 I-V Linearity Analysis

A total of 20 transverse specimens were obtained from each material supplier and have been prepared and tested using the six-probe method. The voltage measured by the top probe, V_t, and bottom probe, V_b, together with the acting current, have been recorded. The measured voltage and current are first used to determine the resistance, R, of the specimen. The obtained resistance data are then used as input to the COMSOL model together with the applied current to determine the voltage value. They are subsequently used to solve Ohm's Law and finally obtain the conductivity values of each specimen.

The data recorded for each voltage sweep are averaged before further analysis. The obtained voltage difference between the top and bottom probes is plotted against the acting current. This has been done for the face-up and face-down measurements and presented in Figure 3.3. According to Ohm's Law, the slope between the voltage and current plot is the electrical resistance of the specimen. The I-V curve shown in Figure 5.2 can be used to verify the Ohmic behaviour of the specimens, which exhibit a constant resistance throughout the measurement. All measured specimens have been found to satisfy the linearity of the I-V curve.

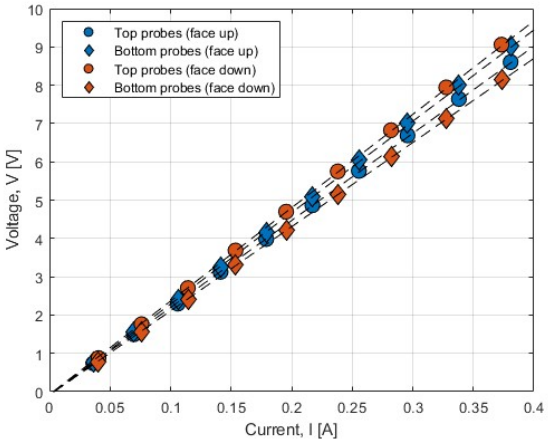

(a) Current and voltage data

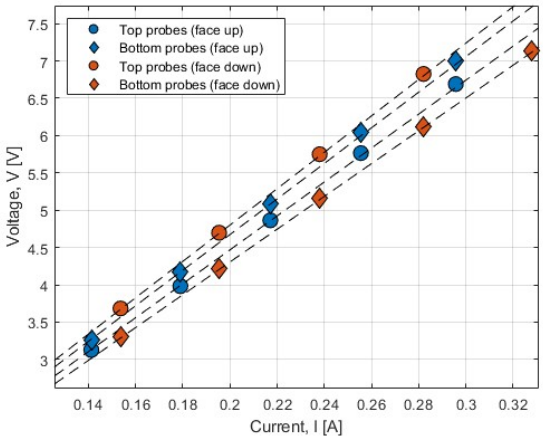

(b) Current and voltage data (zoomed)

Figure 5.2. I-V Linearity analysis of a 32-ply Toray C/PEEK specimen of 15 mm width

The magnification of Figure 5.2 exhibits a deviation between the fitted linear regression. For

measurement labelled as 'face up', the top probe measured a slightly lower voltage reading than the bottom probe, indicating a possibility of non-uniform current density within the specimen. However, during the second measurement, where the specimen is flipped and labelled as 'face down', the top probe showed a higher voltage reading at each measurement increment. The plotted linear regression also shows that the slope for the top probe at 'face up' has a similar value for the bottom probe at 'face down'. This result suggests that there might be a preferential conductive path within the specimen, which could be towards the top or bottom probe, as depicted in Figure 3.3. In the case of data presented in Figure 5.2b, the preferred conductive path might be located near the top probe when the specimen is oriented face up. These preferred conductive paths can be associated with the stochastic nature of the occurrence of fibre contact, which could be higher, allowing more current flow in that region.

The response was further homogenised for all specimens by taking the average fitted resistance at the top, R_t, and resistance at the bottom, R_b. Both values are then compared to find the absolute percentage error. The threshold value for inequality is chosen to be $|R_t/R_b| > 2\%$, in which it is considered that non-uniformity is present within the specimen required to calculate the through-thickness conductivity, σ_z.

5.1.2 Anisotropic Conductivity

The characterisation of the transverse conductivity, σ_2, and through-thickness conductivity, σ_3, has been performed using the numerical model in COMSOL Multiphysics as previously described in Section 3.2.2. The average R_t and R_b for all specimens and the applied current were used as input to calculate the objective function in Equation 3.1 and to solve the nodal voltage. The characterised conductivities in transverse and through-thickness directions for Toray TC1200 and Solvay APC are presented in Figure 5.4. The error bars in the figure represent the standard deviation of the dataset. The collected data from current work are compared with previous research performed by Buser et al. [6] and Grouve et al. [4].

The scatter plot of conductivities for the transverse and through-thickness directions is displayed in Figure 5.3. The plotted sample results are obtained from the 20 specimens from Toray and Solvay material that have been measured using the six-probe method.

As expected, the transverse conductivity, σ_2, is generally higher than the through-thickness conductivity, σ_3, for all materials that are considered. This could be attributed to the anisotropic properties of UD composites. Conductivity is highest in the direction parallel to the fibres, as fibres are typically much more conductive than the matrix. In the UD laminate, the plies are spaced apart by resin-rich region. When the current flows to the through-thickness of the laminate, it encounters more matrix material and, therefore, has to pass through the less conductive matrix, resulting in lower conductivity. This will be discussed in more detail in Chapter 6. In addition, it has also been observed that between suppliers, the Toray specimen exhibits higher conductivity values compared to the Solvay specimens.

When looking at the conductivity values, it can be observed that the average of σ_2 and σ_3 for both materials are slightly lower than the values obtained by Buser et al. [6]. However, the standard deviation indicates that the values are still in a similar range. In comparison, the conductivity measured by Grouve et al. [4] is quite similar to the data collected in the current work. In general, the data shows that, for the same materials, the conductivity values in the transverse and through-thickness directions are in the same magnitude and in good agreement with the earlier work. The more comprehensive data from this current work can be found in Appendix B.

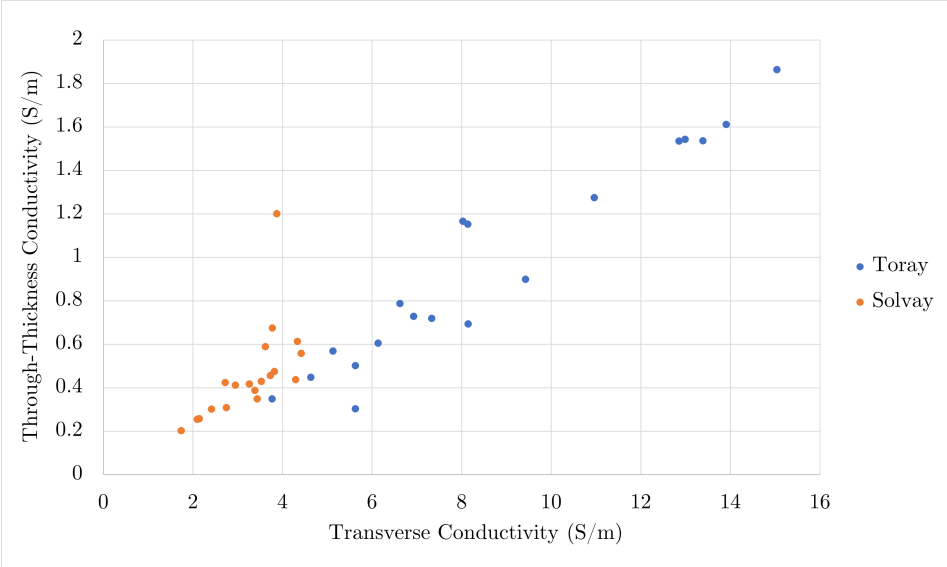

Figure 5.3. Scatter plot of transverse conductivity, σ_2, and through-thickness conductivity, σ_3 of 32-ply UD laminate

5.2 Fibre Radius Calculation

Image analysis techniques have been implemented for a total of 100 micrographs obtained from Toray and Solvay specimens. The histogram provided in Figure 5.5a shows the distribution of fibre radii for Toray material. The x-axis represents the range of fibre radii in micrometers, and the y-axis shows the frequency of fibres observed within each radius range.

From the plot, it is clear that the majority of fibre radii lie between 3.08 and 3.85μm, with the peak frequency observed in the range of 3.38 to 3.54μm. This aligns well with the calculated average fibre radius of 3.39μm and a standard deviation of 0.42μm. The distribution shows a near-symmetrical shape, although slightly skewed towards the larger radii. It is also noteworthy that fibres with radii equal to or exceeding 4μm are less frequent but still present.

Additionally, the error calculated from the ratio of fibre radii equal to or larger than 4μm is found to be 9%. This indicates that only a small proportion of the fibres that fall into this category contribute to the tail observed in the distribution. The presence of this tail, combined with the error measurement, suggests that there is still a fraction of larger fibres within the micrograph. Furthermore, it is important to note that the maximum fibre radius observed in this dataset was 4.62 μm, which indicates that there are fibres that are particularly larger than the average, contributing to the rightward skew in the distribution.

The histogram for the Solvay material, provided in Figure 5.5b, displays a similar trend to that observed in previous materials, with the fibres clustered around the average radius of 3.40μm. The distribution shows a peak in the range of 3.38 to 3.85μm, which is consistent with the calculated mean and the standard deviation of 0.49μm. Similar to the radius distribution found in Toray material, the overall shape is slightly skewed towards larger radii, as indicated by the gradual increase in frequency for radii approaching 4μm and larger, with the maximum fibre radius found equal to 4.62μm. The error, calculated from the proportion of fibres with radii equal to or larger than 4μm, is 12%.

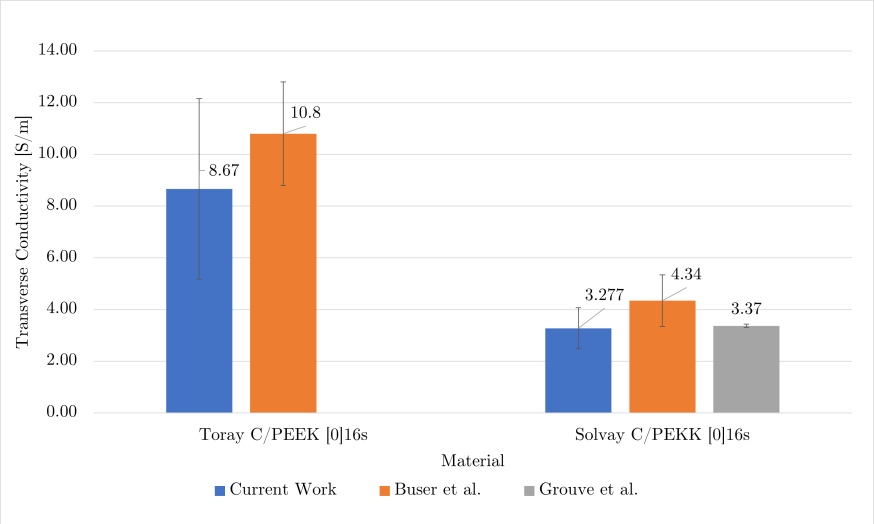

(a) Measured transverse conductivity, σ_2

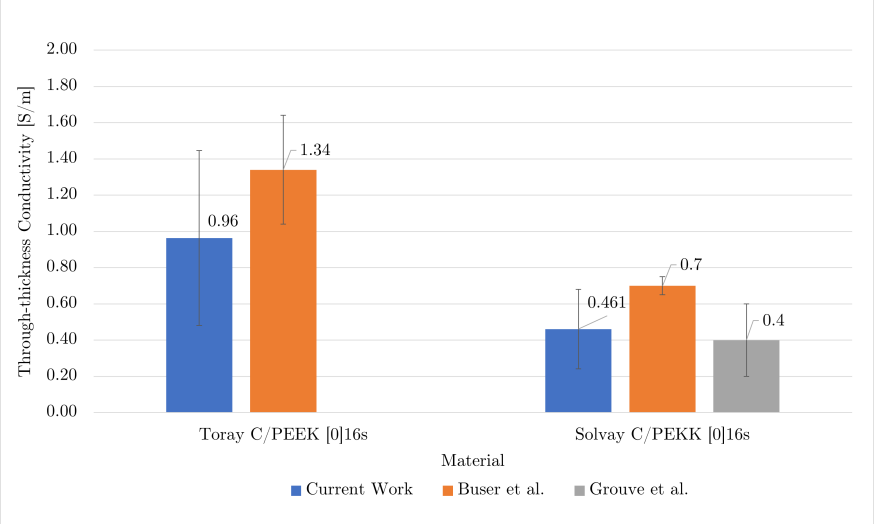

(b) Measured through-thickness conductivity, σ_3

Figure 5.4. Measured conductivities of six-probe samples compared with literature

The radius distribution of Solvay material also shows fibres with radii larger than 4μm. The rightmost bin captures this fraction of fibres, with the maximum fibre radius found being 4.62μm. The error, which is calculated from the proportion of fibres with radii equal to or larger than 4μm to the total number of fibres, is 12%. Overall, the distribution confirms that the majority of fibres in Solvay material conform to the expected range, with a slight variation at the upper end due to the presence of a larger radius fibre radius.

5.3 Nearest Neighbour Analysis

The purpose of this analysis is to observe the arrangement and the interaction of fibre both in the short and long ranges within the given RVE. Four statistical descriptors are utilised to quantify the short- and long-range interactions of fibres: nearest neighbour distance, nearest neighbour orientation, Ripley's K function, and the pair distribution function.

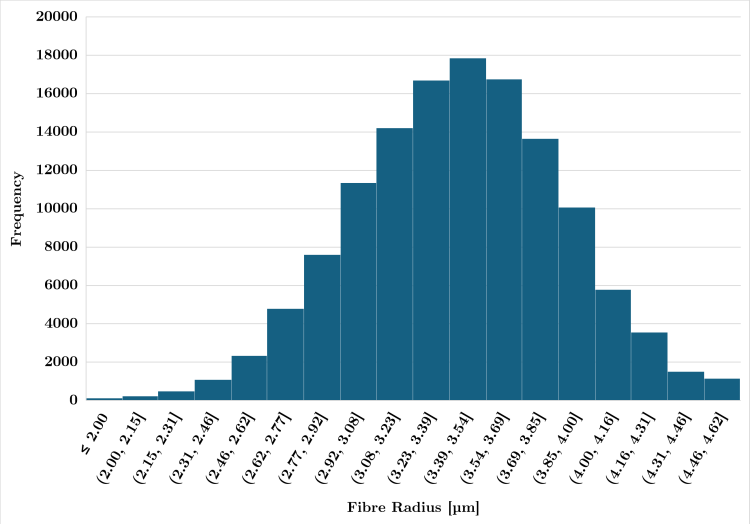

(a) Fibre radius distribution of Toray specimen

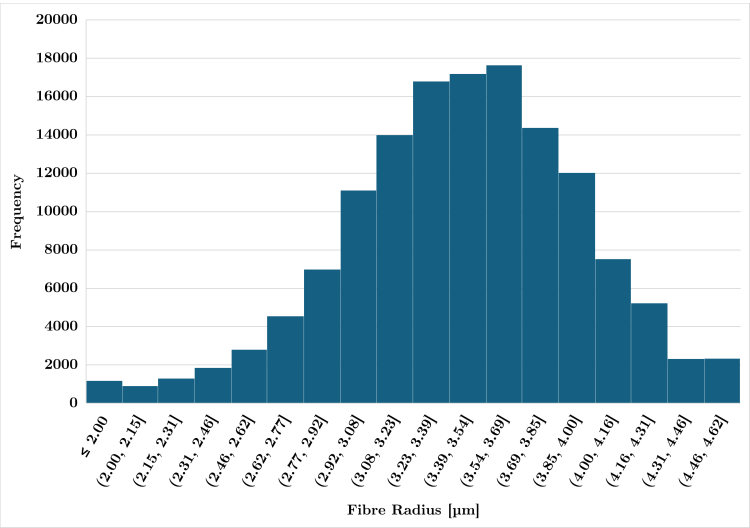

(b) Fibre radius distribution of Solvay specimen

Figure 5.5. Histogram plot of fibre radius distribution obtain from image analysis for Toray and Solvay specimen

5.3.1 Nearest Neighbour Distance

The probability distribution function of first nearest neighbour for Toray and Solvay APC material is presented in Figure 5.6. Error bars is included for each material, indicating the maximum and minimum values for each data point.

As can be observed from the figure, the first nearest neighbour distance for the Solvay micrographs exhibits a peak at a shorter distance compared to the Toray micrographs, with d_{peak} values of 6.58μm for Solvay and 6.80μm for Toray materials, respectively. This suggests that, on average, the Solvay material has a higher likelihood of fibre interaction at short-range distances compared to the Toray material. This is also supported by the fact that the distribution for Solvay APC is broader at a smaller distance, which ranges from 4 to 6μm. In contrast, the distribution for Toray is more concentrated around the peak, with a sharp decline at greater distances. This could indicate greater heterogeneity in the first nearest neighbour distances within the Solvay material.

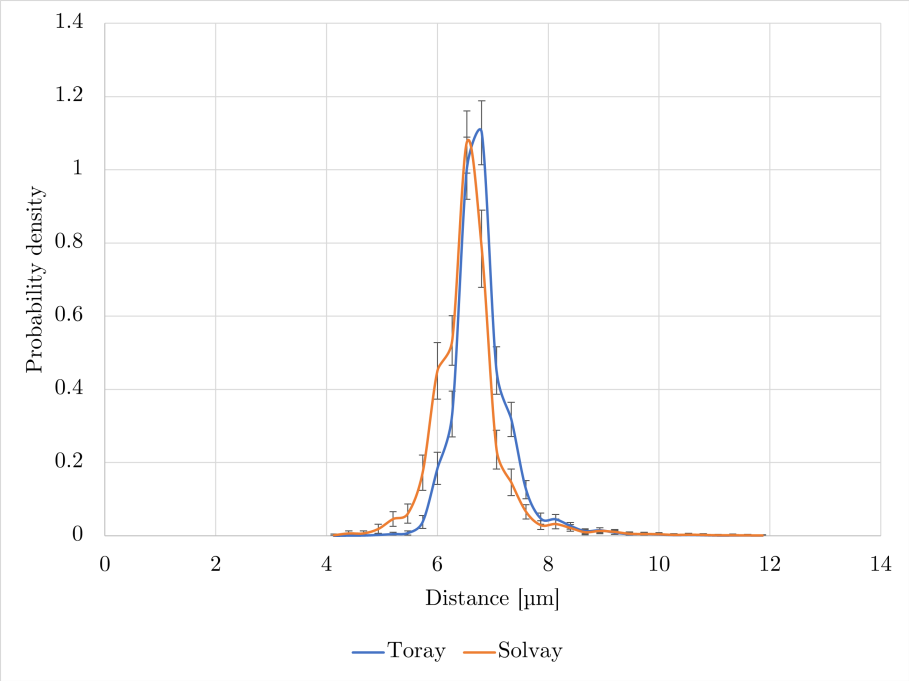

Figure 5.6. Plot of the first nearest neighbour for Toray and Solvay material

Additionally, the slightly higher and narrower peak for Toray might suggest a more uniform, i.e., the nearest neighbour is more evenly spaced than Solvay material.

In addition, the nearest neighbour plot for both materials peaks around 6 to 7 μm, which is approximately twice the average fibre radius of 3.4 μm observed in both materials. This result seems to be appropriate as the nearest neighbour distance is expected to be roughly twice the radius if the fibres are spaced in random distribution. The peak of the nearest neighbour distance distributions aligns with the fibre diameter, which indicates a consistent relationship between fibre diameter and spacing.

5.3.2 Nearest Neighbour Orientation

The cumulative distribution function of the nearest neighbour orientation for Toray and Solvay material is presented in Figure 5.7. Error bars have been included for each material, indicating the maximum and minimum values for each data point. The dashed line represents the CDF for a completely spatially random pattern. In this case, the CDF is linear, which is expected for a random pattern since the probability of finding the nearest neighbour at any orientation is uniform across all angles.

Figure 5.7 illustrates that both the Solvay and Toray materials closely follow the CSR line, indicating that the orientation distribution of nearest neighbours in both materials is nearly random. It can be observed that there are small deviations from the CSR line for both materials, particularly in specific angular ranges, which are around 90° to 135° and 270° to 315°. These deviations suggest slight anisotropies in the nearest neighbour distributions. However, these deviations are not significant enough to imply strong orientation biases.

Overall, the close alignment with the CSR line suggests that any preferred orientation effects are minor. The CDFs for Solvay and Toray material are very similar, with only slight differences seen in certain orientation ranges. This similarity suggests that both materials exhibit comparable

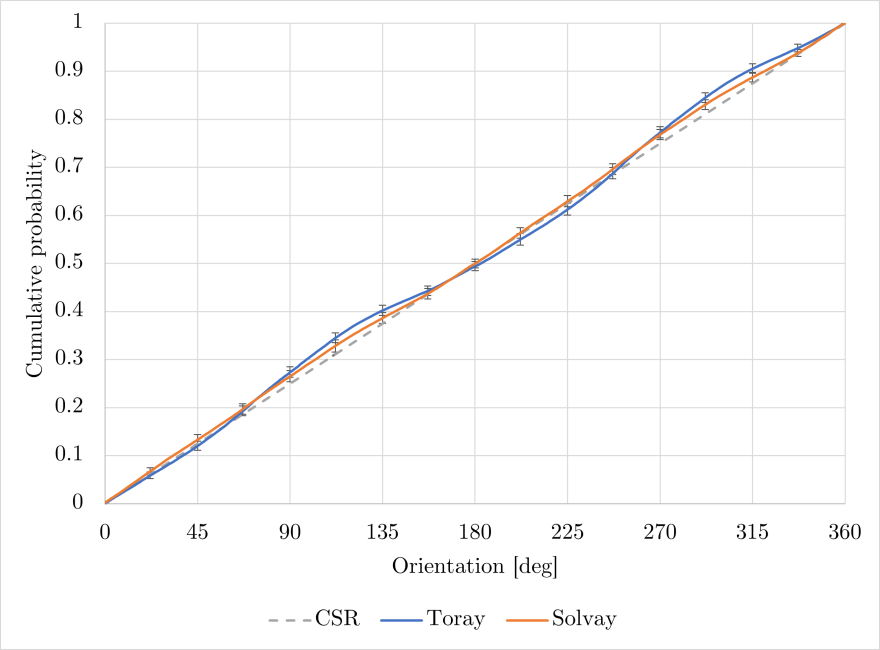

Figure 5.7. Plot of the nearest neighbour orientation for Toray and Solvay material

behaviour in terms of nearest neighbour orientation, with both materials showing no directional preference that deviates from the CSR pattern. This analysis indicates that, from an orientation perspective, both materials exhibit a close to random behaviour, suggesting a lack of preferential orientation in the nearest neighbour arrangements.

5.3.3 Ripley's K Function

The plot of Ripley's K Function for Toray and Solvay material, as well as the CSR pattern, is presented in Figure 5.8.

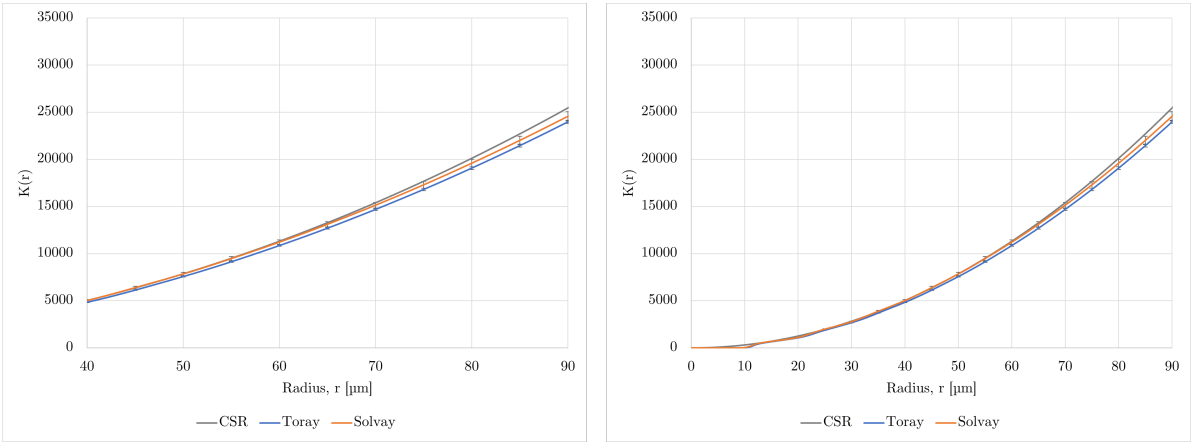

Figure 5.8. Plot of the Ripley's K function for Toray and Solvay material

Figure 5.8 shows the second-order intensity functions for the Toray and Solvay material, compared with the CSR pattern shown with a dashed line. It can be observed that for shorter distances, which range from 0 to 40μm, the Toray and Solvay curves are very close to the CSR curve. While at a certain radius, particularly noticeable at a large distance, the curve for both materials exhibits slight

deviations from the CSR curve. The lower $K(r)$ value for the specimens might be an indication of a slight degree of regularity of fibre distribution in the micrographs compared to randomness.

Furthermore, the $K(r)$values for Solvay and Toray are very similar, with only slight differences visible, indicating that both materials exhibit nearly identical spatial fibre distribution at a distance of up to 40μm. At a larger distance, the Toray curve shows a slightly lower $K(r)$ value than that of the Solvay curve. This might suggest that Toray materials have a more regular or less clustered fibre distribution at higher distances, i.e. the fibre centres are slightly more evenly spaced than in Solvay material, which can be seen in the cross-sectional micrograph of material in Figure 5.1.

Overall, the close distribution of Ripley's K function of both materials to the CSR curve indicates that the spatial distribution of fibre in both materials is nearly random, with only minor tendencies toward regularity at larger distances. This suggests that the microstructure of these materials does not deviate significantly from a random fibre distribution, though there may be small structural differences during the consolidation that can cause small deviations at larger scales.

5.3.4 Pair Distribution Function

The pair distribution function for Toray and Solvay materials compared with the distribution for CSR pattern are shown in Figure 5.9. According to the $g(r)$ distribution, Solvay and Toray materials show similar patterns, exhibiting an oscillatory behaviour. The amplitude of the oscillation decreases with increasing radius. When the radius approaches 30μm, both curves tend to reach the CSR curve with $g(r) = 1$, indicating the fibre distribution becomes more random at larger distances.

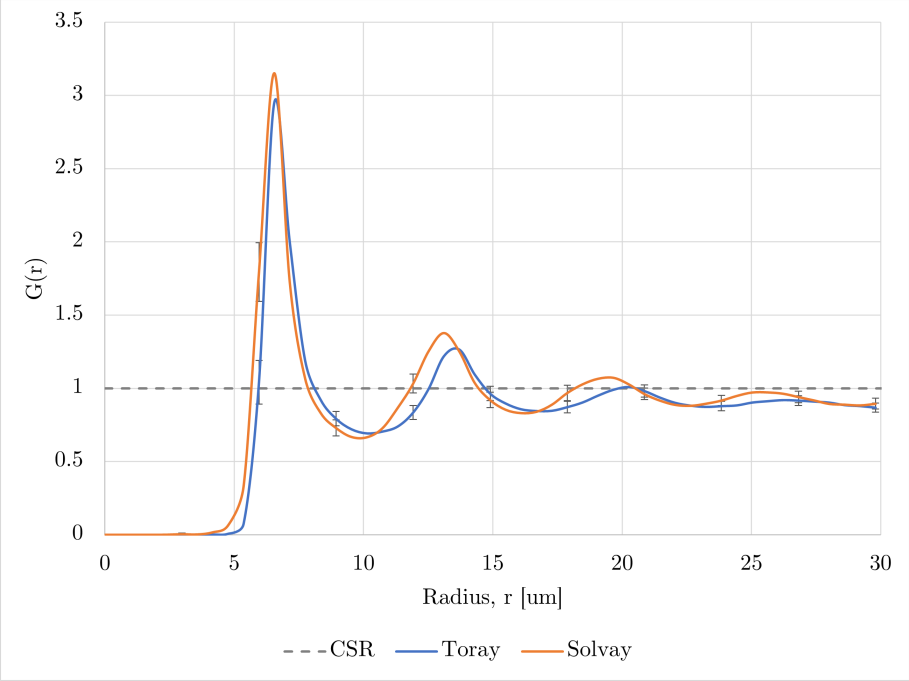

Figure 5.9. Plot of the pair distribution function for Toray and Solvay material

A prominent peak, which is significantly above the CSR curve $g(r) = 1$, was observed at a distance of approximately 6.55 um for both materials, which coincides with the peak of the nearest neighbour distance distribution in Figure 5.6. The peak for Solvay is slightly higher than that of Toray, indicating that at this specific distance, there is a higher degree of clustering of fibres in Solvay compared to Toray material. After the initial decrease, the curves show fluctuations around the

Toray TC1200 ($V_{f,thresh} = 0.25$)					
d_{thresh}	8	9	10	11	12
Transverse	95	100	100	100	100
Through-thickness	400	89	95	97	99

Solvay APC ($V_{f,thresh} = 0.25$)					
d_{thresh}	8	9	10	11	12
Transverse	81	98	99	100	100
Through-thickness	50	83	94	94	96

Table 5.1. Number of conductive paths found in the model with varying d_{thresh}

CSR line, which is typical for high-volume fraction composite [13]. Following the initial peak, both curves decrease below the CSR curve, suggesting a region of reduced probability where fewer fibres are found compared to a random distribution. This implies a degree of regularity at these distances. These oscillations indicate alternating regions of slight clustering (where $g(r) > 1$) and regularity (where $g(r) < 1$).

Overall, Solvay material shows a slightly higher initial peak and generally exhibits a larger deviation from the CSR curve in both the peaks and valleys of the oscillations compared to Toray material. This result suggests that Solvay has a slightly stronger tendency toward both clustering and regularity over these distances.

5.4 Equivalent Resistance Result

Once the boundary points are defined and the largest connected component has been formed, as elaborated in the previous sections, the sets of linear equations can be solved for nodal voltages according to KCL provided in Equation 2.8. Once the equations are solved, one can determine the potential difference of the resistor network and finally obtain the equivalent resistance of the network. In simulating the graph network as an electrical circuit, varying d_{thresh} and $V_{f,thresh}$ values were employed to see the influence of parameters on the generated fibre interaction or the overall network and the output that is calculated equivalent resistance value.

A total of 100 RVEs are evaluated for each material. After the simulating process, it was observed that with varying d_{thresh} and $V_{f,thresh}$, there is a chance that no conductive path from the source to the ground node appears in the model. This absence of conductive paths occurred because no fibre connectivity was found either in the transverse or through-thickness direction, which "disconnected" the main network from either the source or ground node. Non-conductive paths could be interpreted as the material behaving as an insulator at a particular distance. In the case of no conductive paths, the resistance value is theoretically infinite. The number of conductive paths found for each material is presented in Table 5.1 and Table 5.2 for model with varying d_{thresh} and $V_{f,thresh}$, respectively.

To take this non-conductive micrograph into account in the overall calculation of average resistance, a resistance value needs to be assigned for this region. This value is required to reflect the idea that in regions where the material behaves as an insulator, the resistance value would be extremely high. However, it should be noted that careful consideration is required when assigning an appropriate value. In this calculation, an approach of assigning an $R_{no\ path}$ will be taken by choosing a scaling factor, such as

Toray TC1200 (d_{thresh} = 10)					
$V_{f,thresh}$	8	9	10	11	12
Transverse	95	100	100	100	100
Through-thickness	400	89	95	97	99

Solvay APC (d_{thresh} = 10)					
$V_{f,thresh}$	8	9	10	11	12
Transverse	81	98	99	100	100
Through-thickness	50	83	94	94	96

Table 5.2. Number of conductive micrograph found in the model with varying $V_{f,thresh}$

$$R_{no\ path} = f \times R_{max}, \tag{5.1}$$

where f is the scaling factor, and R_{max} is the maximum equivalent resistance value calculated from 100 networks in one particular direction. In this model, f is chosen to be 100, such that the resistance of the non-conductive path is represented and corresponds to a very high resistance compared to that of conductive paths. In calculating average resistance for a particular direction, an approach of utilising the logarithmic scaling was considered. Calculating the average using the logarithmic scaling can help manage the wide range of resistance values, particularly when significant difference in resistance occurs, such as those between conductive and non-conductive values.

When there is a significant disparity between values, e.g. when the resistance for non-conductive micrographs is very high compared to the conductive path resistance, logarithmic scaling can help to bring these values into a more manageable range. The resistance value is the average on a logarithmic scale that can be written as

$$Average\ on\ Log\ Scale = \frac{1}{n}\sum_{i=1}^{n}\log(R_i) \tag{5.2}$$

Subsequently, the logarithmic mean is exponentiated to return to the original scale. The calculated average resistance is different from a simple arithmetic mean and accounts for the impact of high resistances, leading to a more representative average that does not overly skew towards the extreme values. The average equivalent resistance results are plotted in Figure 5.10 and Figure 5.11 for varying inter-fibre spacing threshold, d_{thresh}, and the local fibre volume threshold, $V_{f,thresh}$, respectively.

The influence of varying the parameter of d_{thresh} to the average equivalent resistance can be seen in Figure 5.10a and Figure 5.10b for transverse and through-thickness resistance, respectively. For the transverse direction, both Toray and Solvay show a decreasing trend as the d_{thresh} increases from 8 to 12μm. The transverse resistance for Toray appears to be slightly lower than that for Solvay across all distances, although the difference is not significant.

In terms of the through-thickness resistance, both materials show a sharp decrease as the threshold distance increases. The resistance values drop rapidly from d_{thresh} = 8 to 9μm and then level

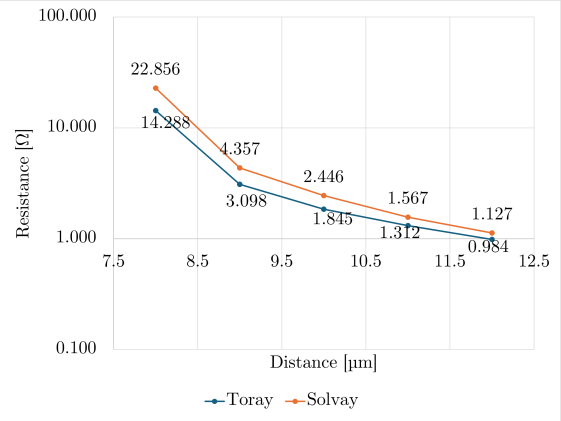

(a) Calculated transverse resistance, R_t, for varying d_{thresh}

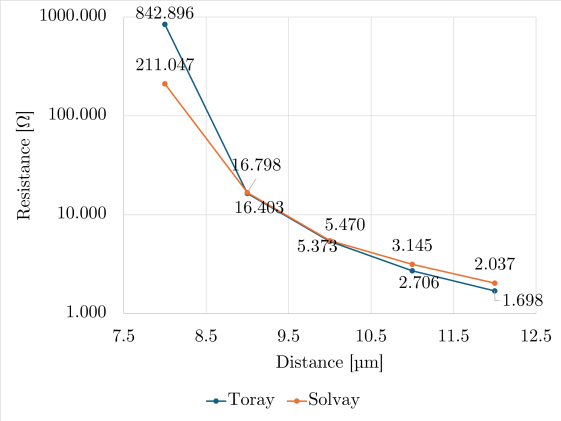

(b) Calculated through-thickness resistance, R_{tt}, for varying d_{thresh}

Figure 5.10. Calculated equivalent resistance from Quasi-3D model with varying d_{thresh}

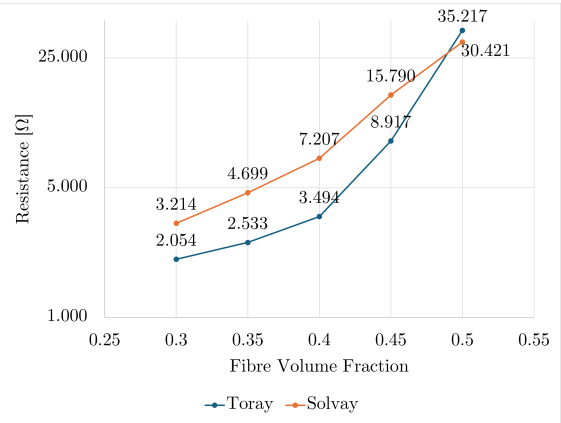

(a) Calculated transverse resistance, R_t, for varying $V_{f,thresh}$

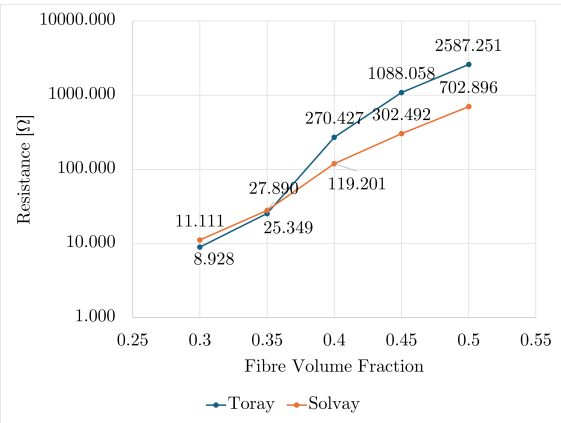

(b) Calculated through-thickness resistance, R_{tt}, for varying $V_{f,thresh}$

Figure 5.11. Calculated equivalent resistance from Quasi-3D model with varying $V_{f,thresh}$

off as the distance increases further. Initially, Toray shows significantly higher through-thickness resistance compared to Solvay at shorter threshold distances, but this difference narrows as the distance increases. In comparison, Solvay exhibits lower resistance at most points, especially at shorter distances.

Furthermore, according to Figure 5.11, the transverse resistance for both Toray and Solvay increases as the $V_{f,thresh}$ increases from 0.3 to 0.5. This indicates that higher $V_{f,thresh}$ correspond to higher transverse resistances. Toray consistently exhibits lower transverse resistance than Solvay across all $V_{f,thresh}$. This might suggest that Toray has better transverse conductivity compared to Solvay, as resistance is inversely related to conductivity. Meanwhile, Solvay shows higher transverse resistance values across the board, which may indicate that its material properties or fibre interaction in a transverse direction results in lower transverse conductivity.

In terms of the through-thickness resistance, both materials exhibit an increase in through-thickness resistance as the $V_{f,thresh}$ becomes higher. The through-thickness resistance is significantly higher than the transverse resistance for both materials, which is typical for UD composite where fibres are aligned in the longitudinal direction that increases the possibility of the absence of a direct

conductive path through-thickness direction. Interestingly, Toray's through-thickness resistance increases sharply with increasing $V_{f,thresh}$ and is generally higher than that of Solvay. According to this calculation, the higher through-thickness resistance for Toray suggests that it is less effective in conducting through the thickness, which is different from the experimental result presented in Section 5.1. These discrepancies in results will be discussed further in Chapter 6.

Chapter 6

Discussion

This chapter discusses the results from the previous chapters. The conductivity results are compared with the morphology of the materials in Section 6.1. The evaluation of the reliability of the image analysis is provided in Section 6.2. Section 6.3 describes the statistical characteristics of the fibre distribution based on 2D cross-sectional micrographs and how it relates to the conductivity. Lastly, the reliability of the current resistor network model is evaluated and presented in Section 6.4.

6.1 Relation of Material Morphology to Conductivity

Figure 5.1 displays the stitched micrograph of the sample morphology representing the two different material suppliers. Additionally, the highly magnified subset of the materials is presented in Figure 6.1. Evaluating the micrographs qualitatively can provide information about the conductive properties of Solvay and Toray materials.

It can be seen that the Toray sample in Figure 5.1a and Figure 6.1a does have a lower amount of matrix material between plies compared to the Solvay samples from Figure 5.1b and Figure 6.1b. In addition, unlike the Solvay material, the ply structure depicted in Figure 5.1a does not display any significant matrix region along the ply in the transverse to the fibre direction. The resin-rich region occurs mainly in the interlaminar part of the material. This could be an indication of more chance of conductive paths along the transverse direction due to the high fibre-to-fibre contact. The Toray samples show higher transverse and through-thickness conductivity compared to Solvay material, as can be observed from the bar plot in Figure 5.4

When observing the Solvay material, fibre clustering is observed, which might indicate a high number of fibre-to-fibre contacts within that region. However, the micrograph also depicts a separation of clusters with matrix material that appears transversely and has remained after consolidation, as can be clearly seen in Figure 6.1b. The lower transverse conductivity of the Solvay samples compared to the Toray samples, as observed in Figure 5.4, may be attributed to these resin-rich regions. The through-thickness conductivity of the Solvay samples is marginally lower than that of the Toray samples. Likewise, the resin-rich regions are also apparent in the through-thickness direction. The resin-rich region seems to be causing the fibre discontinuities reflected in the through-thickness conductivity, which is slightly lower than the Toray samples.

The morphology discussed has been only restricted to the 2D micrographs of the samples. All mechanisms regarding fibre-to-fibre contact that occurs throughout the fibre direction have been excluded. For instance, as seen from a 2D micrograph, two fibres might be in close proximity

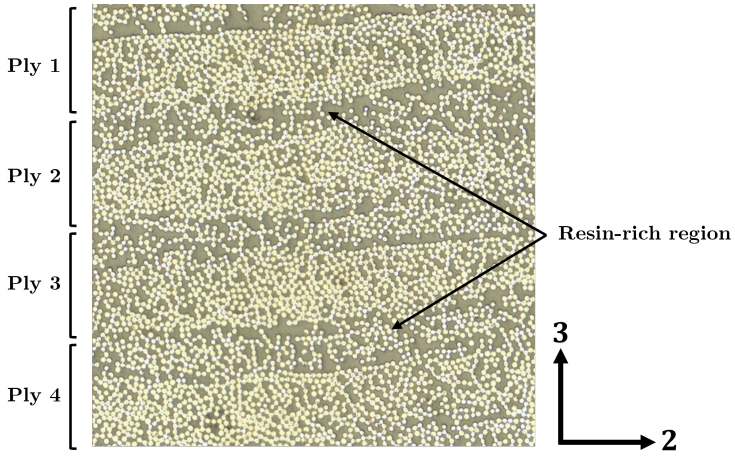

(a) Magnified view of Toray specimen

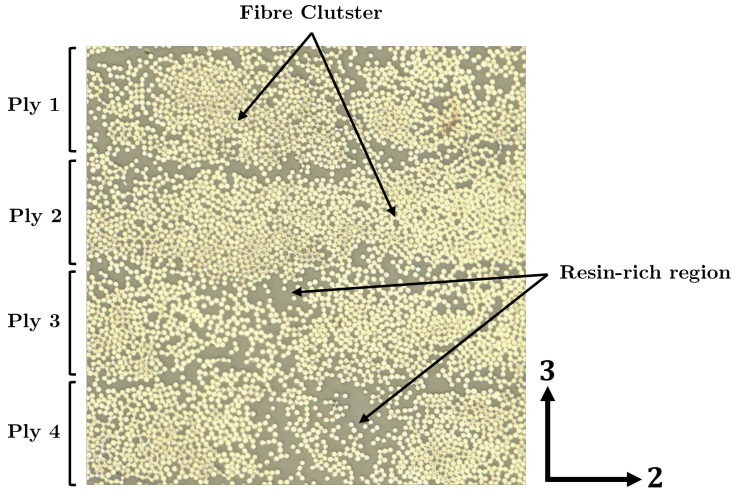

(b) Magnified view of Solvay specimen

Figure 6.1. Micrographs of Toray c/PEEK (left) and Solvay C/PEKK (right) $[0]_{16s}$ consolidated specimens

without making any contact. In practice, however, there could be contact between them at some point throughout the fibre direction.

In relating the transverse and through-thickness conductivities, the scatter plot presented in Figure 5.3 exhibits a diagonal pattern for both Toray and Solvay material, which might be an indication of the relation between σ_2 and σ_3. When measuring a specimen for Toray and Solvay material, the measured conductivity values show some variations for the same material. This phenomenon could be attributed to the local variation of fibre volume fraction that occurs within the laminates. A higher fibre volume fraction could lead to the increase of fibre-to-fibre contact in the fibre direction, which indicates a higher number of conductive paths within the sample, yielding high conductivity along two directions.

Another potential explanation for the observed coupling between through-thickness and transverse conductivity may be related to the morphology of the specimens. For example, the morphology of the Solvay specimens features resin-rich regions that extend both transversely and through the thickness, as illustrated in Figure 5.1b. When an electrical current flows transversely to the fibre direction within the cross-section of the specimens, the current needs to find another conductive path

by moving through the adjacent plies, which might not align directly with the direction where the current flows. This mechanism resulted in a possibly longer conductivity path length and reduced area in the path for the current to flow, resulting in a lower conductivity. The apparent resin-rich regions in the through-thickness direction also imply the low through-thickness conductivity found in Solvay material.

6.2 Image Analysis Technique

Figure 3.12 displays the calculated fibre radii, which are indicated with a green circle. By overlaying this fibre radi obtained from the radius search method, the reliability of the image analysis technique can be evaluated.

In the image analysis technique used in this study, the fibre radius calculation was conducted using the four-direction search method, which generally provides a good approximation of the fibre radius. However, several cases of overestimation were observed, as reflected in measured fibre radii exceeding 4μm in previous results shown in Section 5.2. One possible cause of this overestimation lies in the inaccurate determination of the fibre centre, which was obtained from contour analysis. In some cases, the fibre centre may be slightly off-centre, positioned towards the side of the fibre, as can be seen in Figure 3.9c. This misalignment introduces errors when calculating the radius in four directions, resulting in a fibre radius smaller or larger than what is visually apparent in the micrograph. Such discrepancies highlight the limitations of the method in accurately capturing the centre of irregular fibres.

Additionally, using the watershed algorithm showed limitations when applied to fibres that were unclear or damaged in the micrographs, which can be attributed to specimen preparation issues. In these cases, the algorithm placed the fibre centre between two neighbouring fibres instead of correctly locating the centre of each individual fibre. This misidentification of the fibre centre led to an overestimation of the calculated fibre radius. These limitations emphasize the importance of ensuring careful specimen preparation to obtain good micrograph quality and further refining the fibre detection algorithms, especially for irregular or unclear fibres, to improve the accuracy of the image analysis technique. These instances occur generally in fibres that are located near the micrograph boundary.

Furthermore, after implementing the algorithm on several micrographs from different datasets, it was found that the image analysis technique worked effectively within micrographs having a ratio of μm to pixel, P, ranging from 0.5 to 1.0. It was observed that in micrographs with high resolution, apparent noise or imperfections such as broken fibres could be identified as individual fibres, which influenced the accuracy of the fibre radius calculation and, subsequently, the local fibre volume fraction.

One approach that improved the accuracy of analyzing high-resolution micrographs was to reduce the image size while maintaining the aspect ratio. Figure 6.2 presents the result of fibre radii calculation on several P values. The three micrographs depict cross-sectional images of UD composite fibres with P equals 0.148, 0.296, and 0.592, respectively. These micrographs show several irregular fibres and incomplete fibres at the boundary of the micrographs. Some noises are also apparent in the micrograph, especially with the micrograph having the highest resolution.

In Figure 6.2a, with the lowest ratio, many fibres are detected, especially at the boundaries of the micrograph, where the fibres appear to be incomplete. However, due to the high resolution, neighbouring fibres appear to overlap or intersect. This indicates that the fibre edges may not be clearly defined due to the noise and subtle imperfections captured, which makes it difficult for

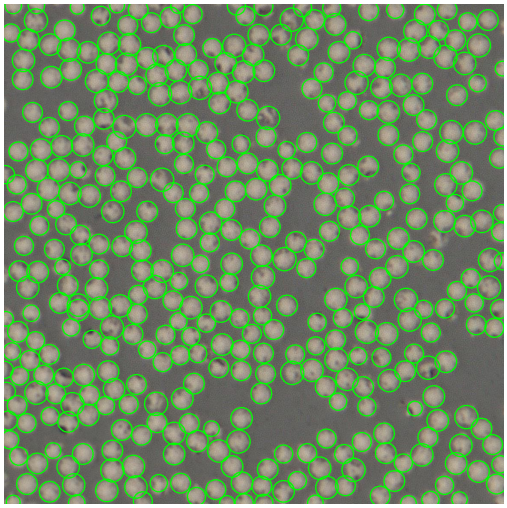

(a) Image analysis with $P = 0.148$

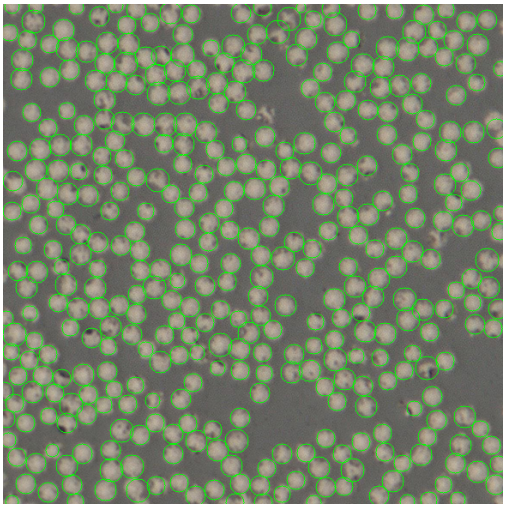

(b) Image analysis with $P = 0.296$

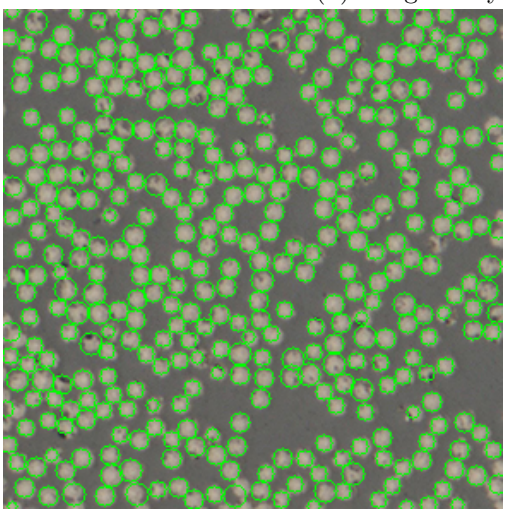

(c) Image analysis with $P = 0.592$

Figure 6.2. Image analysis for fibre radii calculation with varying μm to pixel ratio, P

the algorithm to separate individual fibres. Whereas in Figure 6.2cwith the highest ratio, fewer neighbouring fibres intersect, indicating that the fibre edges are more clearly defined. However, incomplete fibres that are particularly at the boundaries of the micrograph might not be detected as it can be considered as a noise. This occurs because when downsampling an image, the number of pixels is reduced by averaging multiple neighbouring pixels. This can help to smooth out the noise and clarify the separation between the fibre edges and the matrix. In addition, reducing the pixels can also improve the efficiency of the watershed algorithm because it provides clearer contrast between fibres and the background.

This adjustment of micrograph dimensions increases the P ratio to the working range, which improves the detection and calculation process. By lowering the image resolution, the algorithm could segment fibres and matrices in the micrographs more effectively, thus yielding more reliable measurements of the fibre centre and fibre radii. This step highlights the importance of pre-processing image data to optimize the performance of algorithms across different datasets.

6.3 Statistical Characteristics of Materials

The morphology of Toray and Solvay material that was presented in Figure 6.1 has been characterized statistically to quantitatively relate the influence of fibre distribution to the apparent electrical conductivities for both materials. A few key points can be observed by analyzing the statistical descriptors considered and relating the statistics measurement to the measured conductivities.

In principle, the plot of the first nearest neighbour, presented in Figure 5.6, describes how the fibre distribution spreads in the cross-section of the material. The distributions for both materials are quite narrow, indicating that the first nearest neighbour distances are fairly consistent within each material. However, the Solvay distribution appears to have a slightly broader spread at a smaller distance than Toray material, which could imply that the fibres are more clustered in Solvay and more evenly distributed for Toray material.

The nearest neighbour orientation, shown in Figure 5.7, indicates that the slight deviation of the cumulative distribution from the CSR line, specifically in the angle of, could be due to an anisotropic behaviour in the microstructure, 90° to 135° and 270° to 315°, which suggest that the fibres are slightly closer in the through-thickness direction than in the transverse direction. However, since both materials behave similarly, it implies that any structural difference in the consolidation process between them does not significantly affect the orientation of nearest neighbours.

The Ripley's K function and pair distribution function, on the other hand, give details on how clustered the fibre distribution is compared to the CSR pattern. Figure 5.8 and Figure 2.5 present the plot for Ripley's K function and pair distribution, respectively. As can be seen from the figure, the K functions for Solvay and Toray are very similar, with only slight differences visible, indicating that both materials exhibit nearly identical spatial point patterns. The blue line for Toray is slightly below the orange line for Solvay in some regions, suggesting that Toray might have a slightly more evenly spaced or less clustered distribution than Solvay. Meanwhile, the pair distribution function shows that the overall shapes of the curves for Solvay and Toray are quite similar, but there are subtle differences. Solvay shows a slightly higher initial peak and generally exhibits a stronger deviation from CSR in both the peaks and valleys of the oscillations compared to Toray. This might suggest that Solvay has a slightly stronger tendency toward both clustering and regularity over these scales.

When comparing the statistical measurement to the morphology of the samples for Toray and Solvay, it shows that the measurement seems to support the fact that Solvay materials have a more pronounced fibre clustering region separated from the resin-rich region. In contrast, for Toray materials, the measurements suggest that the fibre distribution goes towards more uniformity and is more likely to be well-connected across the material.

Some remarks from this statistical characterization of the microstructure of the material can be drawn. In the transverse direction, the electrical conductivity is heavily influenced by how well the fibres are connected to each other. If fibres are well-distributed and form a continuous network, the transverse conductivity will be higher. If fibres tend to cluster together, as suggested by the initial peaks in the pair distribution function, this could potentially increase local conductivity within the clusters because the fibres are closer together and more likely to form conductive paths. However, if the clustering is too localized, it may reduce overall transverse conductivity by creating regions with poor fibre connections. A more uniform distribution of fibres would typically lead to better transverse conductivity because it ensures that the fibres are well-connected throughout the composite, forming a continuous conductive path.

In Toray material, the pair distribution function shows slightly less clustering, which suggests a more uniform distribution of fibres. This could translate to better transverse electrical conductivity, as the fibres are more likely to be well-connected across the material. On the other hand, Solvay exhibits slightly more pronounced clustering, with the possibility of higher localized conductivity within the clustered regions but potentially with lower overall transverse conductivity if the clusters are isolated from each other.

The key challenge in 2D statistical characterization is that it does not effectively capture long-range effects—such as the presence of resin-rich regions or the overall connectivity of fibre networks over multiple layers in a laminate. It is limited to only assessing the short-range or local distributions. These descriptors are able to give insights into local arrangements of fibres and how fibres are distributed relative to each other at short to medium ranges. However, it fails to assess whether clusters are "isolated" over larger distances, which is crucial for properties like electrical conductivity, especially in the through-thickness direction. This is because 2D statistical descriptors do not account for the 3D connectivity that influences conductivity.

6.4 Quasi-3D Resistor Network

As shown in Section 6.4, the quasi-3D network was modelled from 100 RVEs of each material to calculate the average equivalent resistance. The calculation was done using varying parameters such as the inter-fibre spacing threshold, d_{thresh}, the local fibre volume fraction threshold, and $V_{f,thresh}$ to determine the connectivity of the fibre. The resistance values for transverse and through-thickness are calculated and compared for both materials. The interpretation of the calculated resistance will be elaborated further in this section.

For the first parametric study, the $V_{f,thresh}$ was used as a constant with a value of 0.25 and the varying d_{thresh} ranging from 8 to 12μm. The resistance presented in Figure 5.10 showed that as the distance increases, both Toray and Solvay show a decreasing trend in transverse resistance. This suggests that as distance increases, there is more fibre connectivity within the clustered region of the fibre, implying the current has a more extended path to travel, potentially increasing the cross-section area in which the current flows across the model. It can also be seen that the calculated resistance for Toray material consistently shows a lower resistance than that of Solvay material. A similar trend was also observed when calculating the through-thickness resistance. This trend indicates that longer distances provide more opportunities for current to find paths through the thickness of the specimen, which reduces the overall resistance.

For the second parametric study, the model is generated with a constant d_{thresh} equal to 10μm and varying $V_{f,thresh}$ ranging from 0.3 to 0.5. The resistance calculated from these models is provided in Figure 5.11. When observing the transverse resistance plot, it can be seen that the resistance increases for both materials. The resistance is also observed to be increasing when the threshold value for the local fibre volume fraction increases. However, the calculated resistance seems to be more increasingly pronounced than that in the transverse direction. This highlights that the parameter $V_{f,thresh}$ significantly affects the fibre connectivity in the through-thickness direction, or, in practice, it limits the conductive path between the plies within the laminate.

In order to validate the equivalent resistance result calculated from the quasi-3D resistor network model, it might not be appropriate to directly compare the obtained result with the conductivity value provided in Section 5.1 due to scaling discrepancies within the model and the experimental specimens.

In this model, the resistor network is simplified to only have one contact point for each fibre connectivity and the boundary condition applied in the model, such as the current source, which might be higher than that in the experiment if the cross-sectional area is very small, affecting the resulting resistance calculation obtained from the experiment. Therefore, in comparing the result, the relative trends in which the ratio between the through-thickness resistance, R_{tt} and the transverse resistance, R_t will be compared to the ratio of σ_2 and σ_3 obtained from the experiment. The ratios of R_{tt} and R_t for both materials are shown in Figure 6.3.

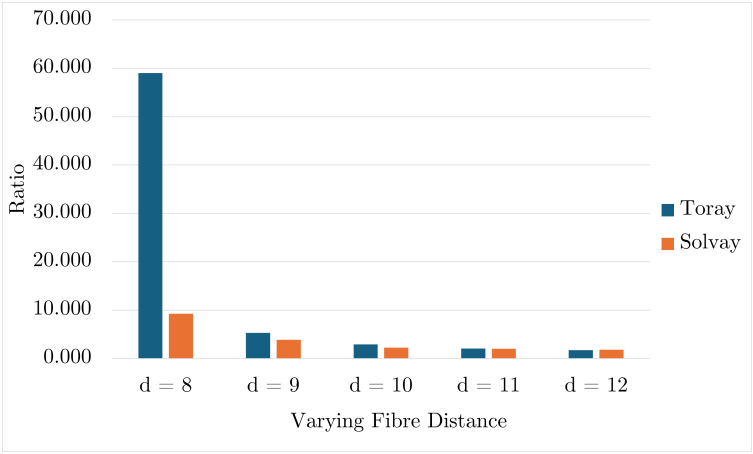

(a) Ratio of R_{tt} and R_t with varying d_{thresh}

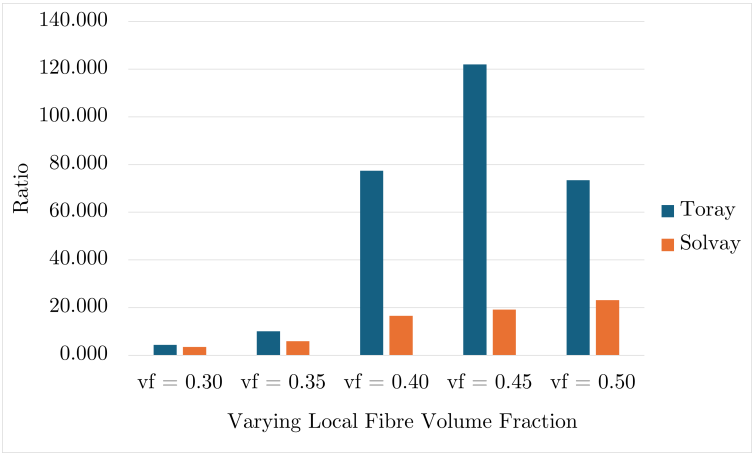

(b) Ratio ofR_{tt} and R_t with varying $V_{f,thresh}$

Figure 6.3. Ratio of equivalent through-thickness resistance, R_{tt}, and transverse resistance, R_t for Toray and Solvay material

When examining Figure 6.3a, the ratio is extremely high for Toray at $d_{thresh} = 8\mu$m, indicating that the through-thickness resistance is significantly higher than the transverse resistance at these shorter distances. As the distance increases, the ratio significantly drops. This suggests that the difference between through-thickness and transverse resistances becomes less pronounced as the distance increases, which could be attributed to longer distances allowing more paths for current to flow, thereby reducing the discrepancies between these two directions. In terms of carrying the $V_{f,thresh}$, the ratio for Toray increases sharply as the $V_{f,thresh}$ increases. This indicates that at a higher threshold, the through-thickness resistance of Toray material becomes much higher relative to its transverse resistance.

The calculated transverse and through-thickness resistance obtained from the model can be related to the number of conductive micrographs found from the RVEs, provided in Table 5.1 and Table 5.2. Toray materials had more paths found in the model for all parametric studies and directions, leading to lower overall resistance compared to Solvay, except for the through-thickness direction at $d_{thresh} = 10\mu$m, where Toray has higher resistance. This discrepancy can be attributed to the fibre distribution. Solvay has a more fibre-clustered region with a significant resin-rich region. Even though fewer conductive paths are found in this material, the current has more contact points to traverse with the clustering region, reducing the equivalent resistance. In contrast, Toray has more uniformly spaced fibres, while resulting in more conductive paths, which might have a smaller effective area for current flow, leading to higher resistance.

Knowing the ratio of σ_2 and σ_3, which is equivalent to 9.03 and 7.10 for Toray and Solvay material, respectively, the parametric value that can be utilized for further modelling is chosen to be d_{thresh} = 10μm and $V_{f,thresh} = 0.35$. This corresponds to the ratio of R_{tt} and R_t from the model 10.00 and 5.93 for Toray and Solvay material, respectively. It is important to note that this model is simplified to having only one contact point in the fibre direction of each fibre connectivity. To enhance the reliability of the calculated equivalent resistance, some improvements in the model can be made for future work.

Chapter 7

Conclusion and Recommendation

7.1 Conclusion

The objective of this thesis is to characterise the transverse and through-thickness conductivity of UD TPCs. The conductivity characterisation for UD TPCs is required as an input when modelling the Induction Welding process of UD TPC material. Furthermore, this thesis also aims to explain the effects of fibre distribution of two distinct materials and relate that to the apparent electrical conductivity, specifically in transverse and through-thickness directions. For this purpose, a microstructure-based quasi-3D model was developed to predict the equivalent resistance value obtained from the micrograph of the material.

The six-probe method was utilised to characterise the electrical conductivity of two materials, Toray and Solvay. The conductivity value seems to be in agreement with previous research. The Toray material has an average transverse and through-thickness conductivity of around $\sigma_2 = 8.67$ S/m and $\sigma_3 = 0.96$ S/m, respectively. Whereas for Solvay material, the average conductivity was around $\sigma_2 = 3.27$ S/m and $\sigma_3 = 0.46$ S/m.

The difference between the morphology of the materials is quantitatively characterised by using the statistical descriptor, such as nearest neighbour, nearest neighbour orientation, Ripley's K function, and pair distribution function. The result showed that the characterisation supports the fact that Solvay materials have a more pronounced fibre clustering region separated by a resin-rich region. In contrast, for Toray materials, the measurements suggest that the fibre distribution goes towards more uniformity and is more likely to be well-connected across the material. A well-distributed fibre network enhances conductivity by forming continuous conductive paths, while localised clustering may improve conductivity within clusters but could reduce overall conductivity due to the separation of resin-rich regions. A uniform fibre distribution generally improves transverse conductivity by ensuring consistent fibre connections throughout the composite. The main limitation of 2D statistical characterisation is its inability to capture long-range effects and connectivity in the fibre direction, making it inadequate for assessing properties, such as through-thickness electrical conductivity, as it only provides insights into local fibre arrangements and short to medium-range distributions.

The quasi-3D network model was used to calculate the average equivalent resistance of 100 RVEs for both Toray and Solvay materials by varying parameters such as inter-fibre spacing threshold, d_{thresh}, and local fibre volume fraction threshold,$V_{fv,thresh}$. It was found that d_{thresh} has a higher influence on defining connectivity within the fibre cluster, whereas $V_{fv,thresh}$ affects through-thickness connectivity. While the model's results are not directly comparable to

experimental conductivity due to simplifications and scaling differences, trends were analysed by comparing resistance ratios. The findings suggest that Toray material has more conductive paths, but the more uniform fibre distribution may lead to higher resistance in certain cases, especially compared to the more clustered fibre arrangement in Solvay material. Based on the experimental and modelled ratios, d_{thresh} of 10μm and $V_{fv,thresh}$ of 0.35 were chosen for further modelling, with recommendations for future improvements to the model.

7.2 Recommendations

Based on the findings of this thesis, a few recommendations for future study could be drawn. The first path would be to explore the influence of the size of the RVE on the computational cost during the modelling of the quasi-3D resistor network. The determination of the RVE size could also contribute to the apparent resin-rich region, which is particularly very distinctive in Solvay material. The larger window size could also provide a better view of connectivity between fibre in case there are separation due to the resin-rich region. The well-defined connectivity could be attributed to the overall equivalent resistance calculation.

The second path would be to explore the influence of extending the quasi-3D resistor network to a full-3D resistor network by incorporating more contact points in the fibre direction. In the current study, only one contact point is implemented, which is a highly simplification of the stochastic nature of the composite laminate. By varying the number of contact points, they could also be referred to as nodes in the fibre direction. By combining this with increasing window size to better capture the effect of resin-rich regions in either transverse or through-thickness directions, a more representative resistance calculation can be obtained, and a reliable model based on the microstructure can be developed.

The last path for the future study could focus on characterising the fibre architecture using 3D micro-CT to provide a more comprehensive 3D view of fibre distribution, which could be useful to assess the connectivity between fibres across the layer that is undetected from a 2D cross-section micrograph. Furthermore, the fibre connectivity obtained from analysing the 3D subset of the specimens can be incorporated when improving the 3D resistor network to help predict the conductivities more accurately.

References

[1] H. Kim, S. Yarlagadda, J. W. Gillespie, N. B. Shevchenko, and B. K. Fink, "A study on the induction heating of carbon fiber reinforced thermoplastic composites," *Advanced Composite Materials*, vol. 11, no. 1, pp. 71–80, Jan. 2002, ISSN: 15685519. DOI: 10.1163/156855102753613309.

[2] Y. M. Buser, W. J. B. Grouve, S. Wijskamp, and R. Akkerman, "Induction Heating of UD C/PAEK-What Thermography Can Teach Us about Eddy Currents," Tech. Rep.

[3] G. Bieleman, "Characteriation of the Through-Thickness Electrical Conductivity of Uni-Directional Themoplastic Composites," Ph.D. dissertation, University of Twente, 2022.

[4] W. Grouve, E. Vruggink, F. Sacchetti, and R. Akkerman, "Induction heating of UD C/PEKK cross-ply laminates," in *Procedia Manufacturing*, vol. 47, Elsevier B.V., 2020, pp. 29–35. DOI: 10.1016/j.promfg.2020.04.112.

[5] Y. M. Buser, W. J. B. Grouve, E. T. M. Krämer, and R. Akkerman, "Electrical Conductivity Characterisation of Stochastic Zigzag Paths In Unidirectional C/PAEK," Tech. Rep.

[6] Y. Buser ab, G. Bieleman ab, W. Grouve, S. Wijskamp, and R. Akkerman ab, "Characterisation of Orthotropic Electrical Conductivity of Unidirectional C/PAEK Thermoplastic Composites," vol. 3, DOI: 10.5075/epfl-298799{_}978-2-9701614-0-0.

[7] J. Zangenberg, J. B. Larsen, R. C. Østergaard, and P. Brøndsted, "Methodology for characterisation of glass fibre composite architecture," in *Plastics, Rubber and Composites*, vol. 41, Jun. 2012, pp. 187–193. DOI: 10.1179/1743289811Y.0000000067.

[8] R. Pyrz, "Quantitative description of the microstructure of composites. Part I: Morphology of unidirectional composite systems," *Composites Science and Technology*, vol. 50, no. 2, pp. 197–208, Jan. 1994, ISSN: 0266-3538. DOI: 10.1016/0266-3538(94)90141-4.

[9] F. J. Guild and J. Summerscales, "Microstructural image analysis applied to fibre composite materials: a review," *Composites*, vol. 24, no. 5, pp. 383–393, Jul. 1993, ISSN: 0010-4361. DOI: 10.1016/0010-4361(93)90246-5.

[10] L. Avérous, J. C. Quantin, D. Lafon, and A. Crespy, "Morphological Determinations of Fiber Composites," *Microscopy Microanalysis Microstructures*, vol. 7, no. 5-6, pp. 433–439, Oct. 1996, ISSN: 1154-2799. DOI: 10.1051/MMM:1996142. [Online]. Available: http://dx.doi.org/10.1051/mmm:1996142.

[11] Y. Hou, K. Zhang, Y. Lu, and A. Noori, "A new strategy for generating regional random fiber-reinforced polymer composite," *International Journal of Mechanical Sciences*, vol. 251, Aug. 2023, ISSN: 00207403. DOI: 10.1016/j.ijmecsci.2023.108346.

[12] W. Wang, Y. Dai, C. Zhang, X. Gao, and M. Zhao, "Micromechanical Modeling of Fiber-Reinforced Composites with Statistically Equivalent Random Fiber Distribution," *Materials*, vol. 9, no. 8, Jul. 2016, ISSN: 19961944. DOI: 10.3390/ma9080624.

[13] T. J. Vaughan and C. T. McCarthy, "A combined experimental-numerical approach for generating statistically equivalent fibre distributions for high strength laminated composite

materials," *Composites Science and Technology*, vol. 70, no. 2, pp. 291–297, Feb. 2010, ISSN: 02663538. DOI: 10.1016/j.compscitech.2009.10.020.

[14] *Scipy Spatial cKDTree*. [Online]. Available: https://docs.scipy.org/doc/scipy/reference/generated/scipy.spatial.cKDTree.html.

[15] W. Wang, H. Wang, S. Fei, H. Wang, H. Dong, and Y. Ke, "Generation of random fiber distributions in fiber reinforced composites based on Delaunay triangulation," *Materials and Design*, vol. 206, Aug. 2021, ISSN: 18734197. DOI: 10.1016/j.matdes.2021.109812.

[16] *Angle Clockwise Between Two Points*. [Online]. Available: https://blog.finxter.com/calculating-the-angle-clockwise-between-2-points/.

[17] L. Yang, Y. Yan, Z. Ran, and Y. Liu, "A new method for generating random fibre distributions for fibre reinforced composites," *Composites Science and Technology*, vol. 76, pp. 14–20, Mar. 2013, ISSN: 02663538. DOI: 10.1016/j.compscitech.2012.12.001.

[18] A. R. Melro, P. P. Camanho, and S. T. Pinho, "Generation of random distribution of fibres in long-fibre reinforced composites," *Composites Science and Technology*, vol. 68, no. 9, pp. 2092–2102, Jul. 2008, ISSN: 0266-3538. DOI: 10.1016/J.COMPSCITECH.2008.03.013.

[19] H. S. Keay, "Application of ring statistics to characterise graphitisation of carbon fiber heat shields under atmospheric re-entry conditions," Tech. Rep.

[20] H. Yu, D. Heider, and S. Advani, "A 3D microstructure based resistor network model for the electrical resistivity of unidirectional carbon composites," *Composite Structures*, vol. 134, pp. 740–749, Dec. 2015, ISSN: 02638223. DOI: 10.1016/j.compstruct.2015.08.131.

[21] M. Soto, M. Esteva, O. Martínez-Romero, J. Baez, and A. Elías-Zúñiga, "Modeling percolation in polymer nanocomposites by stochastic microstructuring," *Materials*, vol. 8, no. 10, pp. 6697–6718, 2015, ISSN: 19961944. DOI: 10.3390/ma8105334.

[22] P. Swart, A. A. Hagberg hagberg, l. -Los, D. A. Schult, and P. J. Swart swart, "Exploring Network Structure, Dynamics, and Function Using NetworkX," Tech. Rep., 2008. [Online]. Available: http://conference.scipy.org/proceedings/SciPy2008/paper_2.

[23] *Multidimensional image processing (scipy.ndimage) — SciPy v1.14.1 Manual*. [Online]. Available: https://docs.scipy.org/doc/scipy/reference/ndimage.html.

[24] M. Couprie, L. Najman, and G. Bertrand, "Algorithms for the topological watershed," *Lecture Notes in Computer Science*, vol. 3429, pp. 172–182, 2005, ISSN: 03029743. DOI: 10.1007/978-3-540-31965-8{_}17.

[25] N. Katuin, D. M. Peeters, and C. A. Dransfeld, "Method for the microstructural characterisation of unidirectional composite tapes," *Journal of Composites Science*, vol. 5, no. 10, Oct. 2021, ISSN: 2504477X. DOI: 10.3390/jcs5100275.

[26] *Carbonfaser-Datenblatt | Hexcel*. [Online]. Available: https://de.hexcel.com/Resources/DataSheets/Carbon-Fiber.

[27] G. Voronoi, "Nouvelles applications des paramètres continus à la théorie des formes quadratiques. Deuxième mémoire. Recherches sur les parallélloèdres primitifs.," *Journal fur die Reine und Angewandte Mathematik*, vol. 1908, no. 134, pp. 198–287, Jul. 1908, ISSN: 14355345. DOI: 10.1515/CRLL.1908.134.198/MACHINEREADABLECITATION/RIS. [Online]. Available: https://www.degruyter.com/document/doi/10.1515/crll.1908.134.198/html.

[28] D. Trias, J. Costa, B. Fiedler, T. Hobbiebrunken, and J. E. Hurtado, "A two-scale method for matrix cracking probability in fibre-reinforced composites based on a statistical representative volume element," *Composites Science and Technology*, vol. 66, no. 11-12, pp. 1766–1777, Sep. 2006, ISSN: 0266-3538. DOI: 10.1016/J.COMPSCITECH.2005.10.030.

[29] *alphashape · PyPI*. [Online]. Available: https://pypi.org/project/alphashape/.

Appendix A

Finitization of Voronoi Cell

A finitization algorithm of a Voronoi cell is performed by creating new finite points that construct Voronoi cells for the cells located on the edge of the micrograph. Subsequently, combining the boundary points of the edges of the micrograph yields a finite Voronoi cell that corresponds to the micrograph boundary fibres. An example of a Voronoi diagram consisting of nine input coordinates, as depicted in Figure A.1, is analysed to describe the finitization algorithm. Here, the input points are illustrated with green dots. The Voronoi vertices are illustrated with orange dots. The black continuous lines represent the Voronoi ridges that construct a finite Voronoi region, whereas the dashed line corresponds to ridges that are going to infinity. The corresponding Voronoi cell numbers (CN) are also denoted for each input point. Note that the numbering of CN is done automatically in the SciPy library and does not necessarily correspond to the order of input points.

The Voronoi tessellation function in the SciPy library provides several outputs, including the coordinates and indices of input Voronoi points and Voronoi vertices. The particular Voronoi vertices construct a Voronoi region which corresponds to the Voronoi cell. By looking at Figure A.1a, it can be seen that several vertices are located out of the analysed x-y plane. These vertices are located at infinity and indicated with index -1.

The Voronoi vertices located at infinity can be finitised by using the following equation:

$$[Finite\ vertex] = [Voronoi\ vertex] + ([Direction] \cdot Radius), \tag{A.1}$$

where the Voronoi vertex is the vertex which is not located at infinity, direction is a direction vector, $\underline{d}$, that indicates the direction of the new finite vertex, and r is the distance of the Voronoi vertex to the new finite vertex. The Voronoi vertex and direction are the 2x1 vectors. The process of finitising the Voronoi vertices is described in more detail in the following paragraphs.

A more detailed view of the lower-left section of the Voronoi diagram is presented in Figure A.1b. The red numbers represent the indices of the Voronoi vertices, where index -1 indicates that the particular vertex lies at infinity. The blue numbers represent the indices of Voronoi ridges. The Voronoi ridge number 1 is used as an example to describe the process of determining the finite Voronoi vertex.

Voronoi ridges can be explained as a line drawn perpendicular to a connecting line between two input points. In the case of Voronoi ridge 1, the line is perpendicular to point 1 and point 2. To determine the direction vector, $\underline{d}$, in Equation A.1, first, a tangent vector, $\underline{t}$, and the normal to the tangent vector, $\underline{n}$, need to be calculated.

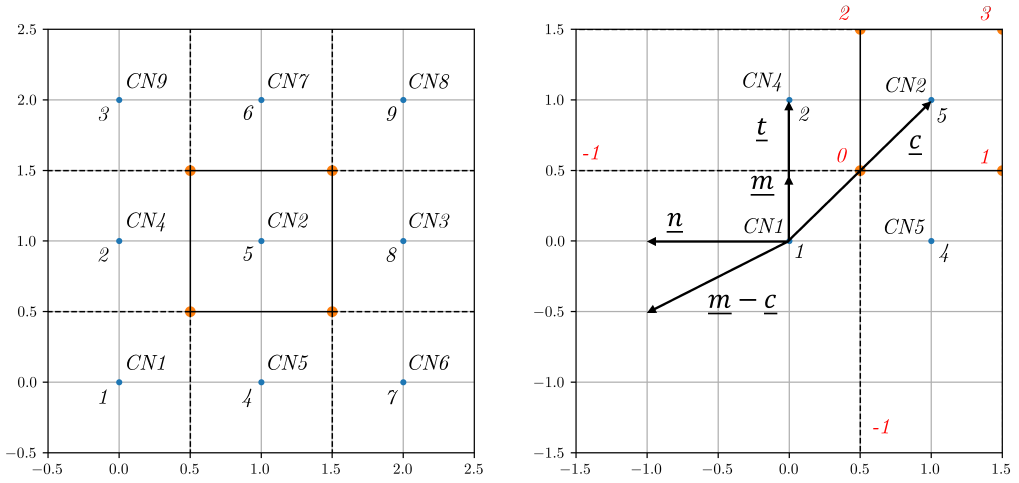

(a) Voronoi diagram consisting of nine points

(b) Detailed view to illustrate the calculation of vectors to determine finite vertex

Figure A.1. Illustration of calculation from infinite to finite Voronoi vertices

A tangent vector, $\underline{t}$, is derived from the vectors of input point 1 and 2, denoted as p_1 and p_2, respectively. The tangent vector can be written as the following

$$\underline{t} = \begin{bmatrix} X_{p_2} \\ Y_{p_2} \end{bmatrix} - \begin{bmatrix} X_{p_1} \\ Y_{p_1} \end{bmatrix} = \begin{bmatrix} 0.0 \\ 1.0 \end{bmatrix}, \tag{A.2}$$

with the normalised tangent vector can be calculated as

$$\hat{\underline{t}} = \frac{\underline{t}}{(|\sqrt{X_t^2 + Y_t^2}|)} = \begin{bmatrix} 0.0 \\ 1.0 \end{bmatrix}. \tag{A.3}$$

The normal vector of $\underline{t}$ is derived by swapping the x- and y-coordinate of $\underline{t}$ and multiplying with -1, which results in

$$\underline{n} = -1 \cdot \begin{bmatrix} Y_t \\ X_t \end{bmatrix} = \begin{bmatrix} -1.0 \\ 0.0 \end{bmatrix}, \tag{A.4}$$

Subsequently, vectors called midpoint and centre vector, referred to as $\underline{m}$ and $\underline{c}$, respectively, are considered to determine the direction vector, $\underline{d}$. The midpoint vector, $\underline{m}$, can be calculated with

$$\underline{m} = \begin{bmatrix} \frac{X_{p_1} + X_{p_2}}{2} \\ \frac{Y_{p_1} + Y_{p_2}}{2} \end{bmatrix} = \begin{bmatrix} \frac{0.0+0.0}{2} \\ \frac{0.0+1.0}{2} \end{bmatrix} = \begin{bmatrix} 0.0 \\ 0.5 \end{bmatrix}. \tag{A.5}$$

The centre vector, $\underline{c}$, is calculated based on the reference point (point 1) and centre of all input points. These centre points can be determined by taking the average of all input points. The direction vector, $\underline{d}$, is calculated using the dot product of vectors m-c and n. If the angle between two vectors is less than 90°, it indicates that the direction in which the finite vertices are created is in the same direction as the normal vector, $\underline{n}$. If the angles are larger and less than or equal to 180°, the finite vertices are in the opposite direction of the normal vector. The radius value needs to be larger than the length of the tangent vector. To take every point into account, the radius values are therefore chosen to be twice the value of the larger fibre x- or y-coordinate. In the case of Figure A.1b, the new finite Voronoi vertex is made starting from the vertex on the finite region (vertex 0), in the direction of $\underline{d}$, with a radius of 4. Hence, the infinite vertex is replaced with a finite vertex at $x = -3.5$ and $y = 0.5$. The process above is repeated for each Voronoi vertex located at infinity. Finally, a finite Voronoi diagram is created.

Appendix B

Experimental Data

The characterization of specimens for Toray and Solvay material has been conducted by utilizing the six-probe method and presented in the following table. The table provides the value of measured resistance from the top probe, R_t, and bottom probe, R_b, obtained from the slope of I-V linearity analysis. The thickness of the specimens, t, was used as input in the COMSOL model, and the calculated conductivity in transverse, σ_2, and through-thickness, σ_3, were compared to the values obtained from the literature.

B.1 Toray TC1200

Sample A (Toray TC1200)											
Sample No.	$R_t[\Omega]$	$R_{t,flip}[\Omega]$	**Avg.** $R_t[\Omega]$	$R_b[\Omega]$	$R_{b,flip}[\Omega]$	**Avg.** $R_b[\Omega]$	t_1 [mm]	t_2 [mm]	t_{avg} **[mm]**	σ_2 **[S/m]**	σ_3 **[S/m]**
A1	22.708	22.920	**22.814**	22.132	22.093	**22.113**	4.604	4.538	**4.571**	**12.988**	**1.544**
A2	22.025	22.243	**22.134**	21.404	21.376	**21.390**	4.604	4.551	**4.578**	**13.388**	**1.537**
A3	53.161	55.436	**54.299**	52.754	49.991	**51.373**	4.504	4.473	**4.489**	**5.625**	**0.502**
A4	48.485	50.225	**49.355**	48.188	46.195	**47.191**	4.516	4.488	**4.502**	**6.137**	**0.606**
A5	44.555	43.268	**43.912**	41.381	43.233	**42.307**	4.463	4.466	**4.465**	**6.930**	**0.730**
A6	42.455	40.627	**41.541**	39.066	40.429	**39.748**	4.475	4.474	**4.475**	**7.334**	**0.720**
A7	37.827	37.346	**37.587**	36.217	37.721	**36.969**	4.462	4.451	**4.457**	**8.026**	**1.167**
A8	37.414	36.663	**37.039**	35.905	36.859	**36.382**	4.468	4.457	**4.463**	**8.140**	**1.153**
A9	21.662	22.078	**21.870**	21.581	20.904	**21.243**	4.446	4.450	**4.448**	**13.908**	**1.612**
A10	19.972	20.378	**20.175**	19.910	19.453	**19.682**	4.452	4.449	**4.451**	**15.035**	**1.864**
A11	31.346	31.210	**31.278**	29.770	29.391	**29.581**	4.685	4.620	**4.653**	**9.423**	**0.900**
A12	36.473	36.346	**36.410**	33.770	34.011	**33.891**	4.691	4.630	**4.661**	**8.146**	**0.694**
A13	63.494	65.827	**64.661**	62.963	60.052	**61.508**	4.586	4.548	**4.567**	**4.630**	**0.448**
A14	76.803	82.352	**79.578**	78.676	71.982	**75.329**	4.592	4.547	**4.570**	**3.769**	**0.350**
A15	50.240	49.962	**50.101**	47.682	49.336	**48.509**	4.531	4.517	**4.524**	**5.627**	**0.304**
A16	58.982	58.126	**58.554**	55.540	57.565	**56.553**	4.527	4.510	**4.519**	**5.128**	**0.569**
A17	58.126	43.474	**50.800**	57.565	44.502	**51.034**	4.496	4.470	**4.483**	**5.841**	**12.135**
A18	46.631	44.497	**45.564**	43.477	45.105	**44.291**	4.493	4.470	**4.482**	**6.623**	**0.788**
A19	22.738	24.370	**23.554**	23.852	21.973	**22.913**	4.464	4.469	**4.467**	**12.851**	**1.535**
A20	26.136	29.181	**27.659**	28.483	25.235	**26.859**	4.460	4.467	**4.464**	**10.961**	**1.276**
Average			**40.425**			**38.833**			**4.516**	**8.667**	**0.963**
Std. Deviation			**16.365**			**15.456**			**0.066**	**3.496**	**0.483**

Table B.1. Experimental data obtained from six-probe measurement of Toray TC1220 for measured resistance at top probe, R_t, bottom probe, R_b, specimen thickness, t, calculated transverse conductivity, σ_2, and through-thickness conductivity, σ_3

B.2 Solvay APC

Sample B (Solvay APC)											
Sample No.	$R_t[\Omega]$	$R_{t,flip}[\Omega]$	**Avg.** $R_t[\Omega]$	$R_b[\Omega]$	$R_{b,flip}[\Omega]$	**Avg.** $R_b[\Omega]$	t_1 [mm]	t_2 [mm]	t_{avg} **[mm]**	σ_2 **[S/m]**	σ_3 **[S/m]**
B1	82.457	82.035	**82.246**	79.822	80.738	**80.280**	4.420	4.388	**4.404**	**3.726**	**0.457**
B2	69.269	69.044	**69.157**	67.052	68.160	**67.606**	4.427	4.402	**4.415**	**4.417**	**0.558**
B3	103.530	105.276	**104.403**	102.914	102.480	**102.697**	4.371	4.372	**4.372**	**2.946**	**0.413**
B4	86.561	88.016	**87.289**	84.416	86.006	**85.211**	4.386	4.389	**4.388**	**3.524**	**0.429**
B5	96.606	91.661	**94.134**	92.360	91.924	**92.142**	4.389	4.397	**4.393**	**3.259**	**0.417**
B6	81.192	79.914	**80.553**	80.125	79.574	**79.850**	4.404	4.411	**4.408**	**3.772**	**0.675**
B7	91.259	88.391	**89.825**	85.208	87.763	**86.486**	4.400	4.405	**4.403**	**3.436**	**0.349**
B8	72.929	70.529	**71.729**	67.928	70.180	**69.054**	4.415	4.415	**4.415**	**4.291**	**0.438**
B9	140.350	144.880	**142.615**	141.208	136.788	**138.998**	4.411	4.426	**4.419**	**2.143**	**0.258**
B10	123.444	128.683	**126.064**	125.129	121.130	**123.130**	4.421	4.434	**4.428**	**2.417**	**0.303**
B11	69.766	68.385	**69.076**	66.780	68.837	**67.809**	4.508	4.479	**4.494**	**4.336**	**0.614**
B12	90.356	87.463	**88.910**	85.019	87.226	**86.123**	4.522	4.492	**4.507**	**3.381**	**0.388**
B13	84.031	82.100	**83.066**	81.367	82.727	**82.047**	4.469	4.467	**4.468**	**3.615**	**0.589**
B14	110.853	109.896	**110.375**	109.361	108.312	**108.837**	4.477	4.468	**4.473**	**2.720**	**0.424**
B15	76.311	77.829	**77.070**	76.056	77.830	**76.943**	4.478	4.471	**4.475**	**3.870**	**1.202**
B16	108.390	111.492	**109.941**	109.855	111.511	**110.683**	4.475	4.468	**4.472**	**2.703**	**5.051**
B17	79.213	79.307	**79.260**	77.230	77.427	**77.328**	4.463	4.456	**4.460**	**3.819**	**0.476**
B18	108.466	112.995	**110.731**	107.987	106.635	**107.311**	4.460	4.452	**4.456**	**2.745**	**0.310**
B19	141.377	146.888	**144.133**	142.800	137.939	**140.370**	4.461	4.476	**4.469**	**2.098**	**0.255**
B20	171.537	177.237	**174.387**	172.665	166.203	**169.434**	4.457	4.471	**4.464**	**1.738**	**0.204**
Average			**99.211**			**96.929**			**4.437**	**3.277**	**0.461**
Std. Deviation			**29.128**			**28.214**			**0.039**	**0.790**	**0.219**

Table B.2. Experimental data obtained from six-probe measurement of Solvay APC for measured resistance at the top probe, R_t, bottom probe, R_b, specimen thickness, t, calculated transverse conductivity, σ_2, and through-thickness conductivity, σ_3

Appendix C

Analysis of Variance of Toray Material

The analysis of variance (ANOVA) has been performed on the micrograph of Toray specimens. In the study, ten micrographs with varying window sizes ranging from 100 to 500 μm were considered and evaluated for three parameters such as fibre density, fibre volume fraction obtained directly from the micrographs, and fibre volume fraction obtained from the area of Voronoi cells.

C.1 Fibre Density

Fiber Density (FD)									
Window Size [μm]	100	150	200	250	300	350	400	450	500
Window Area [μm^2]	10000	22500	40000	62500	90000	122500	160000	202500	250000
FD 1	0.0140	0.0140	0.0139	0.0145	0.0144	0.0144	0.0146	0.0144	0.0143
FD 2	0.0146	0.0150	0.0145	0.0149	0.0146	0.0142	0.0143	0.0141	0.0141
FD 3	0.0156	0.0139	0.0145	0.0142	0.0136	0.0139	0.0139	0.0140	0.0139
FD 4	0.0137	0.0140	0.0148	0.0138	0.0145	0.0146	0.0143	0.0147	0.0148
FD 5	0.0129	0.0146	0.0153	0.0135	0.0141	0.0144	0.0143	0.0145	0.0147
FD 6	0.0138	0.0155	0.0148	0.0140	0.0142	0.0143	0.0139	0.0140	0.0144
FD 7	0.0140	0.0144	0.0143	0.0150	0.0148	0.0145	0.0145	0.0143	0.0142
FD 8	0.0150	0.0146	0.0136	0.0149	0.0148	0.0148	0.0148	0.0146	0.0144
FD 9	0.0154	0.0136	0.0136	0.0145	0.0147	0.0148	0.0148	0.0152	0.0148
FD 10	0.0142	0.0143	0.0148	0.0145	0.0140	0.0145	0.0143	0.0144	0.0150

Table C.1. Calculation of fibre density of Toray TC1200 material

Source of Variation	SS	df	MS	F-value	P-Value	F-crit
Between Groups	1.64E-07	8	2.05E-08	0.085527	0.999511	2.054882
Within Groups	1.94E-05	81	2.4E-07			
Total	1.96E-05	89				

Table C.2. ANOVA results for fibre density parameter of Toray TC1200 material

C.2 Fibre Volume Fraction (Image)

Fibre Volume Fraction Image (FVF)									
Window Size [μm]	100	150	200	250	300	350	400	450	500
FVF 1	0.512	0.523	0.512	0.540	0.539	0.531	0.541	0.531	0.526
FVF 2	0.530	0.537	0.510	0.541	0.523	0.504	0.505	0.504	0.507
FVF 3	0.543	0.477	0.511	0.496	0.479	0.505	0.493	0.489	0.484
FVF 4	0.519	0.522	0.555	0.522	0.553	0.557	0.534	0.555	0.554
FVF 5	0.450	0.537	0.563	0.481	0.523	0.534	0.535	0.545	0.550
FVF 6	0.493	0.555	0.542	0.500	0.506	0.526	0.500	0.503	0.515
FVF 7	0.522	0.534	0.559	0.568	0.551	0.532	0.541	0.524	0.525
FVF 8	0.547	0.529	0.487	0.560	0.565	0.558	0.548	0.532	0.529
FVF 9	0.570	0.474	0.519	0.538	0.546	0.552	0.544	0.570	0.557
FVF 10	0.526	0.561	0.548	0.537	0.519	0.537	0.535	0.546	0.591

Table C.3. Calculation of fibre volume fraction obtained from micrograph of Toray TC1200 material

Source of Variation	SS	df	MS	F-value	P-Value	F-crit
Between Groups	0.001296	8	0.000162	0.229392	0.984443	2.054882
Within Groups	0.057193	81	0.000706			
Total	0.058488	89				

Table C.4. ANOVA results for fibre volume fraction (image) parameter of Toray TC1200 material

C.3 Fibre Volume Fraction (Voronoi)

Fibre Volume Fraction Voronoi (FVF)									
Window Size [μm]	100	150	200	250	300	350	400	450	500
FVF 1	0.545	0.560	0.553	0.576	0.579	0.569	0.578	0.570	0.565
FVF 2	0.560	0.569	0.549	0.576	0.561	0.545	0.543	0.543	0.546
FVF 3	0.579	0.522	0.545	0.538	0.526	0.545	0.534	0.527	0.520
FVF 4	0.567	0.570	0.595	0.567	0.591	0.593	0.572	0.591	0.589
FVF 5	0.487	0.575	0.594	0.517	0.560	0.566	0.568	0.579	0.584
FVF 6	0.529	0.588	0.570	0.534	0.543	0.562	0.538	0.542	0.552
FVF 7	0.582	0.578	0.597	0.605	0.592	0.568	0.581	0.564	0.565
FVF 8	0.583	0.563	0.524	0.593	0.602	0.592	0.582	0.565	0.562
FVF 9	0.604	0.514	0.558	0.571	0.580	0.587	0.575	0.596	0.586
FVF 10	0.572	0.600	0.583	0.572	0.562	0.579	0.575	0.583	0.624

Table C.5. Calculation of fibre volume fraction obtained from Voronoi cells of Toray TC1200 material

Source of Variation	SS	df	MS	F-value	P-Value	F-crit
Between Groups	0.000796	8	9.95E-05	0.156058	0.995737	2.054882
Within Groups	0.051628	81	0.000637			
Total	0.052424	89				

Table C.6. ANOVA results for fibre volume fraction (Voronoi) parameter of Toray TC1200 material

6% Overall Similarity

Top sources found in the following databases:

- 4% Internet database
- Crossref database
- 0% Submitted Works database
- 4% Publications database
- Crossref Posted Content database

TOP SOURCES

The sources with the highest number of matches within the submission. Overlapping sources will not be displayed.

1	research.utwente.nl Internet	<1%
2	mdpi.com Internet	<1%
3	Nico Katuin, Daniël M. J. Peeters, Clemens A. Dransfeld. "Method for t... Crossref	<1%
4	ris.utwente.nl Internet	<1%
5	Soto, Matias, Milton Esteva, Oscar Martínez-Romero, Jesús Baez, and ... Crossref	<1%
6	Lei Yang, Ying Yan, Zhiguo Ran, Yujia Liu. "A new method for generatin... Crossref	<1%
7	Weiwei Wang, Han Wang, Shaohua Fei, Haijin Wang, Huiyue Dong, Ying... Crossref	<1%
8	lirias.kuleuven.be Internet	<1%

9	utwente on 2024-06-28 Submitted works	<1%
10	repositorio-aberto.up.pt Internet	<1%
11	plantcell.org Internet	<1%
12	research.nottingham.edu.cn Internet	<1%
13	Taotao Zhang, Ying Yan. "A comparison between random model and p... Crossref	<1%
14	utwente on 2024-04-01 Submitted works	<1%
15	mafiadoc.com Internet	<1%
16	dokumen.pub Internet	<1%
17	researchgate.net Internet	<1%
18	Sun Won Kim, Jae Hyuk Lim, Seong Su Kim. "Enhanced prediction of tr... Crossref	<1%
19	Shin-Mu Park, Jae Hyuk Lim, Myeong Ryun Seong, Dongwoo Sohn. "Eff... Crossref	<1%
20	mdpi.com Internet	<1%

21	Valentin Romanov, Stepan V. Lomov, Yentl Swolfs, Svetlana Orlova, Lar... Crossref	<1%
22	carmelab.huji.ac.il Internet	<1%
23	link.springer.com Internet	<1%
24	lutpub.lut.fi Internet	<1%
25	coursehero.com Internet	<1%
26	M Thomas. "Estimation of effective thermal conductivity tensor from c... Crossref	<1%
27	Wallison Angelim Medeiros, Guilherme Aris Parsekian, Armando Lopes... Crossref	<1%
28	Aram Bahmani, Ramin Yousefi Nooraie, Thomas L. Willett, John Monte... Crossref	<1%
29	E.P.J. Tozer. "Broadcast Engineer's Reference Book", Routledge, 2012 Publication	<1%
30	Francesco Zangrossi, Fang Xu, Nick Warrior, Petros Karapappas, Xiang... Crossref	<1%
31	utwente on 2024-08-26 Submitted works	<1%
32	Florentius Johannes van Zanten, Harikrishnan Mohan, Darun Barazanc... Crossref	<1%

33	Hong Yu, Dirk Heider, Suresh Advani. "A 3D microstructure based resis... Crossref	<1%
34	M. Thomas, N. Boyard, L. Perez, Y. Jarny, D. Delaunay. "Representative... Crossref	<1%
35	amslaurea.unibo.it Internet	<1%
36	engrxiv.org Internet	<1%
37	C. McCarthy, T. Vaughan. "Micromechanical failure analysis of advanc... Crossref	<1%
38	Guilherme Hideo Tubone. "3D Facial Reconstruction from Point Clouds... Crossref posted content	<1%
39	Krishna Prasad Vadrevu, K. V.S. Badarinath. "Spatial pattern analysis o... Crossref	<1%
40	University of Twente on 2024-10-07 Submitted works	<1%
41	arno.uvt.nl Internet	<1%
42	d-nb.info Internet	<1%
43	dspace.lib.cranfield.ac.uk Internet	<1%
44	eprints.whiterose.ac.uk Internet	<1%

45	matec-conferences.org Internet	<1%
46	"The Structural Integrity of Carbon Fiber Composites", Springer Nature,... Crossref	<1%
47	Bernardo Lejano, Kenneth Jae Elevado, Maria Angelika Fandiño, Ethan ... Crossref	<1%
48	Bohdana Marvalova, Iva Petrikova. "Constitutive Models for Rubber IX",... Publication	<1%
49	Carlone, Pierpaolo, and Gaetano S. Palazzo. "A Micro-Scale Model for ... Crossref	<1%
50	Jameel Khan, Sandy Smith, Paul Tuohy, Matthieu Gresil, Constantinos ... Crossref	<1%
51	Kishore Debnath, Inderdeep Singh. "Primary and Secondary Manufactu... Publication	<1%
52	M.V. Pathan, V.L. Tagarielli, S. Patsias, P.M. Baiz-Villafranca. "A new al... Crossref	<1%
53	Y.M. Buser, E.T.M. Krämer, R. Akkerman, W.J.B. Grouve. "Induction hea... Crossref	<1%
54	pure.manchester.ac.uk Internet	<1%
55	udspace.udel.edu Internet	<1%
56	utwente on 2021-05-19 Submitted works	<1%

57	nlsinfo.org Internet	<1%

Excluded from Similarity Report

- Bibliographic material
- Manually excluded sources
- Small Matches (Less then 10 words)

EXCLUDED SOURCES

utwente on 2024-10-17

Submitted works

99%